Time-dependent model of creep on the Hayward fault from joint inversion of 18 years of InSAR and surface creep data

M. Shirzaei[1,2] and R. Bürgmann[2]

[1]   Spatial and temporal variations of aseismic fault creep influence the size and timing of large earthquakes along partially coupled faults. To solve for a time-dependent model of creep on the Hayward fault, we invert 18 years of surface deformation data (1992–2010), obtained by interferometric processing of 52 and 50 SAR images acquired by the ERS1/2 and Envisat satellites, respectively, and surface creep data obtained at 19 alinement and 4 creepmeter stations. For multi-temporal analysis of the SAR data we developed a method for identifying stable pixels using wavelet multi-resolution analysis. We also implement a variety of wavelet-based filters for reducing the effects of environmental artifacts. Using a reweighted least squares approach, we inverted the interferometric data to generate a time series of surface deformation over the San Francisco Bay Area with a precision of better than a few millimeters. To jointly invert the InSAR displacement time series and the surface creep data for a time-dependent model of fault creep, we use a robust inversion approach combined with a Kalman filter. The time-dependent model constrains a zone of high slip deficit that may represent the locked rupture asperity of past and future M≈7 earthquakes. We identify several additional temporal variations in creep rate along the Hayward fault, the most important one being a zone of accelerating slip just northwest of the major locked zone. We estimate that a slip-rate deficit equivalent to Mw 6.3–6.8 has accumulated on the fault, since the last event in 1868.

1.   Introduction

[2]   The Hayward fault, extending for about ~70 km onshore of the eastern San Francisco Bay area, accommodates ~25% of the relative motion between the Pacific and Sierra Nevada—Great Valley plates (Figure 1 and e.g., *d'Alessio et al.* [2005]). This fault has shown distinct phases of activity including large coseismic ruptures (such as a ~Mw6.8 earthquake in 1868), frequent microseismicity, and aseismic creep [e.g., *Lienkaemper et al.*, 1991; *Toppozada and Borchardt*, 1998; *Waldhauser and Ellsworth*, 2002]. *Savage and Lisowski* [1993] relate the rate of stress accumulation to the surface creep rate using a frictional model and estimated a strain accumulation rate equivalent to a Mw6.8 event per century. Considering a bigger fault rupture area, *Lienkaemper and Galehouse* [1998] doubled the estimate

of the Hayward fault's seismic potential. Relying on a paleoseismic, 1900-yr earthquake chronology of the 12 most recent earthquakes, *Lienkaemper et al.* [2010], determined a 161 ± 65 yr mean recurrence interval and suggest a ~29% (±6%) chance for a large event by 2040.

[3]   Surface creep is observed along the complete 70-km long onshore extent of the Hayward fault. Given the long-term slip rate of 9 ± 2 mm/yr, 30–90% of this rate is accommodated by aseismic creep at the surface [*Lienkaemper et al.*, 1991, 1997]. *Simpson et al.* [2001] attribute the along-strike variations of surface creep rates to changes in the depth extent of creep. Using boundary element models of a stress-free shallow fault driven by slip below the seismogenic zone, they find that creep reaches to depths of 4–12 km on the Hayward fault. *Bürgmann et al.* [2000] consider similar models and also conclude that creep extends deeper along the northern ~20 km and southern ~10 km of the fault. Viscoelastic finite element models in which the shallow fault creep is driven by distributed viscous shear below the seismogenic zone suggest that to explain the pattern of surface creep, only a single, smaller locked patch near the central section of the Hayward fault is needed [*Malservisi et al.*, 2003]. Using a local recurrence-time method based on the size-frequency distribution of micro-earthquakes, *Wyss* [2001] mapped the subsurface location of potentially locked and unlocked patches on the Hayward fault, identifying a central locked asperity near Hayward. Using Global
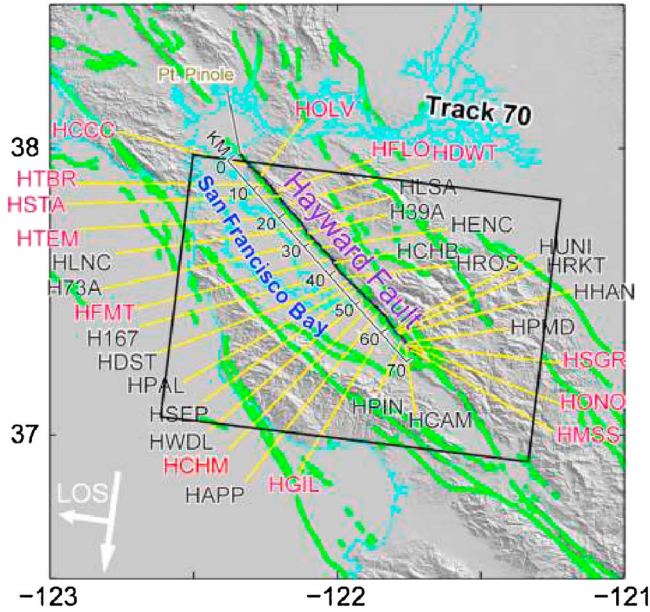

Figure 1. Study area. The trace of the Hayward fault (black line) as well as the location of the alignment stations is marked. Trace of other major faults is marked in green. The black box shows the approximate ground footprint of the SAR frame used in this study. Shaded relief topography is from SRTM (Shuttle Radar Topography Mission) DTM (Digital Train Model). The stations marked with red are not used in this study due to very poor temporal resolution. Shorelines are marked in cyan.

Positioning System (GPS) data and two European Remote-Sensing (ERS) interferograms, *Bürgmann et al.* [2000] estimate that ~7 mm/yr creep extends to near the base of the seismogenic zone along the northern segment of the Hayward fault. Joint inversion of GPS, interferometric synthetic aperture radar (InSAR), and seismic data sets using elastic dislocation theory reveals two locked patches between depths of 8–12 km located near the southern end of the Hayward fault and between 10 and 30 km distance from Pt. Pinole [*Schmidt et al.*, 2005], which is located on the shore of San Pablo Bay (see Figure 1). *Funning et al.* [2005] use a more extensive InSAR data set to invert for a single locked asperity at depth reaching from Berkeley to Fremont. *Evans et al.* [2012] invert for regional fault slip rates and distributed creep on the Hayward fault relying on a block model approach. Their geodetic long-term slip rate estimate is 6.7 ± 0.8 mm/yr, their model creep rates generally increase with depth and they infer peak slip-deficit rates of ~4 mm/yr in the upper 5 km of the fault near Hayward and below 5 km depth near Pt. Pinole.

[4] The creeping behavior of the Hayward fault also varies due to perturbation of the regional stress field induced by seismic events, such as the 1989 Loma Prieta earthquake [*Lienkaemper et al.*, 1997]. Following this event, surface creep on the southern Hayward fault slowed down and stopped on one segment, for about 6 years. In February of 1996, the quiescence was ended by a rapid creep event of 25–30 mm followed by a slow recovery phase and surface creep rates are only now approaching the pre-Loma Prieta rate [*Lienkaemper et al.*, 2012]. Using a spring-slider and a

boundary element model of fault creep with a rate- and state-dependent friction rheology, *Kanu and Johnson* [2011] suggest that this creep event extended to a depth of ~4–7.5 km. *Lienkaemper et al.* [2012] report another slow slip event at km ~20–35 from Point Pinole following the 2007 Oakland Mw4.2 earthquake. This event continued for several days and was characterized by a logarithmic decay of slip over ~100 days [*Lienkaemper et al.*, 2012].

[5] The Hayward fault creep partially releases the accumulating stress aseismically and thus limits the magnitude and changes the recurrence times of large earthquakes. The size and distribution of eventual coseismic slip influences the amplitude and distribution of strong ground motion and the associated hazard [*Aagaard et al.*, 2010]. Moreover, the spatiotemporal variation of creep rates reflects changes in loading of the locked fault sections. Therefore, characterizing the spatiotemporal distribution of the Hayward fault creep is of importance for developing a more accurate and time-dependent earthquake hazard assessment. To this end, we generate a long time series of the surface deformation using interferometric synthetic aperture radar (InSAR) images acquired by ERS1, 2, and Envisat satellites measuring the surface deformation over the Bay Area during the period of 1992–2010. Using a time-dependent inverse modeling scheme that combines re-weighted L2-norm minimization and a Kalman filter, we jointly invert InSAR and surface creep time series to obtain the spatiotemporal distribution of the Hayward fault creep. This time-dependent model allows for constraining the source regions of several creep events and points to the location of potential future seismic events.

2. Methods

2.1. InSAR Time Series

[6] Considering $N + 1$ SAR scenes acquired over the same area at time steps $(t_0, t_1, \ldots, t_N)$ with nearly identical viewing geometry, we generate k interferograms with a perpendicular orbit baseline of less than a certain value (here 400 m). Due to phase decorrelation processes, not all pixels contain useful information. Therefore, a procedure to identify stable pixels is implemented as follows.

2.1.1. Elite Pixel Identification

[7] Our method for identifying stable (i.e., less noisy) pixels involves the statistical assessment of the time series of the interferometric phase noise. The interferometric phase noise in the real domain can be expressed as an additive noise model [*Lee et al.*, 1998];

$$\varphi_z = \varphi_x + r \tag{1}$$

where φ_x is the true phase and r is the additive zero-mean noise depending on interferometric phase coherence (ρ) and number of looks (n). Considering the interferometric phase as a point on a unit circle, its representation in the complex domain is

$$e^{j\varphi_z} = \cos(\varphi_z) + j\sin(\varphi_z) \qquad j = \sqrt{-1} \tag{2}$$

[8] The noise is estimated by using wavelet packet analysis [*Goswami and Chan*, 1999] of the complex interferometric phase [*Lopez-Martinez and Fabregas*, 2002]. The phase

noise is obtained by denoising the complex interferometric phase and subtracting it from the original phase (for more detail on the denoising step, see [*Lopez-Martinez and Fabregas*, 2002; *Shirzaei*, 2012]). A Gaussian scattering model for the distribution of the scatterers is assumed and a scale-dependent soft thresholding scheme is used [*Goswami and Chan*, 1999; *Han et al.*, 2007]. This method obtains the denoising criterion based on the variance of the wavelet coefficients and thus does not need any a priori information.

[9] In the following, the estimated real ($\widehat{r}^{\,c}$) and imaginary ($\widehat{r}^{\,s}$) series of interferometric phase noise for a pixel at location $x = (\zeta, \eta)$ in k interferograms is $\left\{ \widehat{r}_1^c(\xi, \eta) + j\widehat{r}_1^s(\xi, \eta), \right.$ $\widehat{r}_2^c(\xi, \eta) + j\widehat{r}_2^s(\xi, \eta), \ldots, \widehat{r}_k^c(\xi, \eta) + j\widehat{r}_k^s(\xi, \eta) \right\}$ with the associated temporal variance of $\left\{ \sigma_c^2 + j\sigma_s^2 \right\}$, where $\sigma_{c,s}^2 = {}^1\!/_{k-1} \sum_i^{k-1} \widehat{r}_i^{c,s}$. Given the relation between the interferometric phase and complex phase observations, $\varphi_z = \tan^{-1}({}^{\mathrm{Im}}\!/_{\mathrm{Re}})$ where Im and Re are the imaginary and real parts, respectively, the standard deviation of the interferometric phase is as follows:

$$\sigma^\varphi(\xi, \eta) = \sqrt{\left(\frac{\partial \varphi_z}{\partial \mathrm{Im}} \sigma_s(\xi, \eta) \right)^2 + \left(\frac{\partial \varphi_z}{\partial \mathrm{Re}} \sigma_c(\xi, \eta) \right)^2} \quad (3)$$

where σ^φ is the interferometric phase noise and ∂ denotes a partial derivative. Assuming the reference variance of σ for the interferometric phase, the following statistic is valid [*Vanicek and Krakiwesky*, 1982];

$$\frac{(k-1)\sigma^{\varphi^2}}{\sigma^2} \sim \chi_{k-1}^2 \quad (4)$$

where χ^2 is the chi-square probability density functions. By specifying a significance level of α, the confidence interval for σ^φ can be expressed as

$$\sigma^{\varphi^2} < \frac{\sigma^2}{(k-1)} \chi_{k-1, 1-\alpha/2}^2 \quad (5)$$

[10] Passing this test is the criterion for being an elite pixel. σ can be estimated based on an expected variance for the Line of Sight range change (L_R) as follows:

$$\varphi_z = -\frac{4\pi}{\lambda} L_R$$
$$\sigma^2 = \left(-\frac{4\pi}{\lambda} \sigma_l \right)^2 \quad (6)$$

where λ is the radar wavelength and σ_l is the standard deviation of the L_R displacement (e.g., 5 mm).

[11] Following the stable pixel selection step, we apply phase unwrapping of the interferometric phase of a network of sparse elite pixels using a minimum cost flow approach [*Costantini*, 1998; *Costantini and Rosen*, 1999; *Shirzaei*, 2012]. Before this step and to improve the phase quality, an adaptive low-pass filter is applied to noisy interferograms [*Goldstein and Werner*, 1998]. After phase unwrapping, we correct every interferogram for the spatially correlated component of atmospheric delay using the method proposed by [*Shirzaei and Bürgmann*, 2012] and we also remove the possible error due to the inaccuracy of the orbital parameters following [*Shirzaei and Walter*, 2011].

2.1.2. Time Series Generation

[12] The absolute phase values measured in each interferogram and converted to displacements ($\delta\phi_{ab}$) between acquisitions a and b can be related to the surface motion as follows:

$${}^q\delta\phi_{ab} = \psi_b - \psi_a \quad , \quad 1 \leq q \leq k \quad , \quad 1 \leq a \leq N-1 \quad , \quad a < b \leq N \quad (7)$$

where $\psi = [\psi_1, \ldots, \psi_N]^T$ is the vector of N unknown displacements and $\delta\phi = \left[{}^1\delta\phi, \ldots, {}^k\delta\phi \right]^T$ is the vector of k known unwrapped phase observations associated with a pixel at coordinates (ζ, η). Equation (7) can be expressed in matrix form as

$$A\hat{\psi} = \delta\phi - \varepsilon_{\bar{\phi}} \quad (8)$$

where A is the sparse design matrix with dimension of $k \times N$, containing -1 and $+1$ values corresponding to slave and master images in each interferogram, ε_ϕ is observation error, and $\hat{\psi}$ is the estimated displacement time series. Due to, for instance, phase unwrapping errors and the effects of atmospheric delay, observations are contaminated with outliers. Thus, to solve equation (8), we may apply a robust approach such as L_1-norm minimization [*Marshall and Bethel*, 1996]. Implementing the L_1-norm approximation requires rigorous mathematical calculations that lead to a linear or quadratic programming problem using Gauss-Markov models [*Amiri-Simkooei*, 2003; *Marshall and Bethel*, 1996]. A simpler result, similar to applying L_1-norm approximation, can be obtained through robust regression [*O'leary*, 1990]. This approach applies iterative weighted least squares (ILS), with observation reweighting as a function (e.g., bisquare) of the residuals from the previous step [*O'leary*, 1990]. The advantage of this approach is that it allows for reducing the weight of outliers following iterations [*Lauknes et al.*, 2011]. To start the ILS approach, we consider the least squares solution of equation (8) as [*Mikhail*, 1976];

$$\hat{\psi} = \left(A^T P A \right)^{-1} A^T P \delta\bar{\phi} \quad (9)$$

where $()^T$ and $()^{-1}$ are the transpose and inverse matrix operators and in case of independent but temporally overlapping subsets one should replace the simple inverse with the general inverse operator [*Bjerhammar*, 1973; *Pepe et al.*, 2005]. P is the weighting matrix and is proportional to the inverse of the square of the phase noise estimated in section 2.1.1. The iterations of the ILS begin following estimating new weights for observations as follows [*Holland and Welsch*, 1977; *O'leary*, 1990];

$$Q^i = W^i P \quad , \quad i = 1, 2, \ldots$$
$$Q^0 = P$$
$$W_{11}^i = {}^1\!/_{\left(1 + (R_l^i)^2 \right)}$$
$$R_l^i = V_l^{i-1} \!/_{(T \times S_{i-1})}$$
$$S_{i-1}^2 = {V^{i-1}}^T Q^{i-1} V^{i-1} \!/_{d_f}$$
$$V^i = \delta\phi - A\hat{\psi}^i \quad (10)$$

where T is a tuning factor (here 2.385 after *Holland and Welsch* [1977]), df is the degree of freedom (number of

interferograms − number of images + 1), S^2 and Q are the variance factor and updated observation weighting matrix, and W is a down-weighting factor. The updated parameters are obtained as

$$\hat{\psi}^i = \left(A^T Q^i A\right)^{-1} A^T Q^i \delta\phi \tag{11}$$

[13] The statistical properties of this estimation are detailed in *Huber* [1981]. The procedure of calculating the new weight and updating parameters is repeated until a predefined stopping criteria is reached. The stopping criteria used here is as follows:

$$\left|\hat{\psi}^i - \hat{\psi}^{i-1}\right| < \delta \tag{12}$$

where δ is a small number (e.g., 10^{-7}). Following m iterations, the full variance-covariance matrix of the displacement time series can also be obtained by *Mikhail* [1976]:

$$\Sigma_{\hat{\psi}\hat{\psi}} = S_m{}^2\left(A^T Q^m A\right)^{-1} \tag{13}$$

where S_m^2 and Q^m are the final variance factor and weight matrix after the stopping criteria is reached. In case of independent but temporally overlapping data sets, such as combining ERS and Envisat acquisitions, the simple inverse in equation (11) is replaced by a generalized inverse operator [*Bjerhammar*, 1973; *Pepe et al.*, 2005]. Having obtained the time series of surface motion, we are able to further reduce temporal high frequency noise, which mostly includes atmospheric delay. To this end, we use a spatial high-pass and temporal low-pass filter [*Ferretti et al.*, 2001; *Shirzaei*, 2012].

2.2. Time-Dependent Fault Creep Modeling

[14] To relate the time series of surface displacement to the kinematics of the spatio-temporal distribution of creep on the Hayward fault, we devise a time-dependent inverse modeling scheme [*Shirzaei and Walter*, 2010]. This method consists of two main operators (1) a robust optimization algorithm such as L1-norm minimization as a minimum spatial mean error estimator [*Marshall and Bethel*, 1996], and (2) a linear Kalman filter (LKF) [*Grewal and Andrews*, 2001] as a minimum temporal mean square error estimator to generate time series of the creep for each triangular dislocation of the fault-interface mesh. These two steps are implemented iteratively [*Shirzaei and Walter*, 2010]. In this study, we assume that surface deformation is due to pure strike slip on triangular dislocation sources [*Meade*, 2007] that are buried in an elastic, homogenous half-space medium with shear modulus and Poisson ratio of 3×10^{10} Pa and 0.25, respectively. At each time step t, the mathematical relation between surface deformation observation (τ_t) and fault creep (μ_t) is as follows:

$$\tau_t + z_t = B\mu_t \quad , \quad P_t = S_0^2 \Sigma_{\tau_t\tau_t}^{-1}$$
$$lb_t \le \mu_t \le ub_t \quad , \quad t = 1, 2, \ldots \tag{14}$$

where $[\tau_t(x_1,y_1), \tau_t(x_2,y_2), \ldots, \tau_t(x_n,y_n)]^T$ are the observations of the surface displacement at surface locations of $\{(x_i,y_i)\}_{i=1:n}$ (here, surface deformation obtained from InSAR data (τ_{t1}) following the algorithm detailed in section 2.1 and surface creep data (τ_{t2})). $\mu_t = [\mu_t(\theta_1,\beta_1), \mu_t(\theta_2,\beta_2), \ldots, \mu_t(\theta_m,\beta_m)]^T$ is the creep at the patch located at $\{(\theta_i,\beta_i)\}_{i=1:m}$ along strike and dip of the fault, B is the design matrix that includes Green's functions relating fault

dislocation to the surface displacements (and unit vectors projecting 3-D surface displacement into satellite line of sight (LOS) observations), z_t is the vector of observation residuals, $\Sigma_{\tau_t\tau_t}$ is the variance-covariance matrix of the observations, S_0^2 is the primary variance factor, and lb_t and ub_t are lower and upper bounds for the resolved creep at each patch at time t [*Mikhail*, 1976].

[15] To obtain an optimum creep model, equation (14) is solved subject to an objective function, such as L2-norm minimization of the observation residuals. To reduce the effects of outliers, such as non-tectonic signals including hydrology and uncompensated contributions from other fault systems, we implement a robust optimization scheme involving a reweighted L2-norm as described in section 2.1.2 for InSAR time series generation. To reduce the roughness of the slip distribution on the fault plane and avoid unrealistic stress heterogeneities, we minimize the second-order derivative of the fault creep as an additional constraint (e.g., *Segall and Harris* [1987]):

$$\gamma D\mu_t = 0 \tag{15}$$

where D is the Laplacian operator and γ is the smoothing factor determining the roughness of the optimum creep model that we discuss in more detail in the next section. Thus, the final system of equations is rewritten in matrix form as follows:

$$\begin{pmatrix} \tau_t \\ 0 \end{pmatrix} + \begin{pmatrix} z_t \\ 0 \end{pmatrix} = \begin{pmatrix} B \\ \gamma D \end{pmatrix} \mu_t$$
$$lb \le \mu_t \le ub \quad , \quad t = 1, 2, \ldots, N$$
$$pt \|P_t z_t\|_{L_2} \to \min \tag{16}$$

[16] Following optimization of the slip model for observation times $\{t_1, t_2, \ldots, t_N\}$ and determination of a time series of the creep and the associated variance-covariance for each patch, we apply the LKF to reduce temporal noise. The LKF addresses the problem of estimating the parameters of a linear, stochastic system with measurements that are linear functions of the parameters. Given the time series of creep $\{\mu_1, \ldots, \mu_N\}$ for a patch located at (θ_j, β_j) and the associated variance-covariance matrix of $\Sigma_{\mu\mu}$, according to the original form of the LKF, the system dynamics and measurement models, respectively, are formulated as follows [*Grewal and Andrews*, 2001]:

$$\mu_t = \Phi_{t-1}\mu_{t-1} + f_{t-1} \quad , \quad f_t \sim N(0, F_t)$$
$$U_t = H_t\mu_t + g_t \quad , \quad g_t \sim N(0, G_t) \quad , \quad t = 1, 2, \ldots \tag{17}$$

where q and r are Gaussian-distributed noise and Φ and H are $N \times N$ matrices, $F_t = G_t$, and U_t is the measured slip at time t that is obtained by solving the system of equation (16). A recursive solution for the system of equation (17) can be generated as follows [*Shirzaei and Walter*, 2010]:

$$\widehat{\mu_t^+} = \widehat{\mu_t^-} + \bar{Y}_t\left[z_t - H_t\widehat{\mu_t^-}\right]$$

$$P_t^+ = \left[I - \bar{Y}_t H_t\right]P_t^-$$

$$\widehat{\mu_t^-} = \Phi_{t-1}\widehat{\mu_{t-1}^+}$$

$$P_t^- = \Phi_{t-1}P_{t-1}^-\Phi_{t-1}^T + F_{t-1} \tag{18}$$

$$\bar{Y}_t = P_t^- H_t^T \left[H_t P_t^- H_t^T + G_t\right]^{-1}$$

In equation (18), $\widehat{\mu_t^+}$ and P_t^+ are the final estimates of the slip and the associated variance-covariance matrix, respectively.
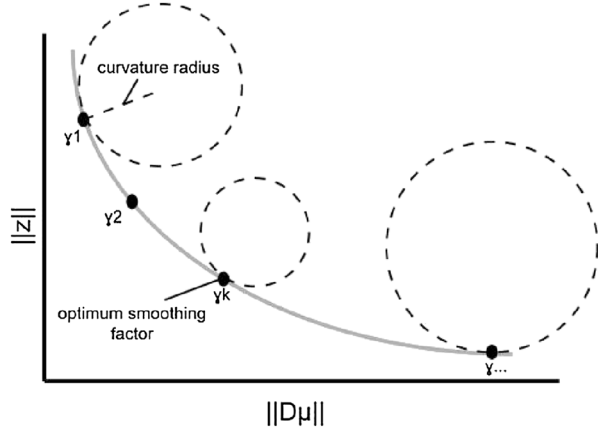
Figure 2. Schematic view of the method for estimating the optimum smoothing factor using the curvature of the tangent circle at any point on a plot of misfit and roughness for a given smoothing factor. The D is the Laplacian operator, μ is the fault slip, z is the observation residual, γ is the smoothing factor, and $\| \|$ is the norm operator.

2.3. Automatic Estimation of the Smoothing Factor

[17] The smoothing factor γ is a function of the number of observations and the associated variance-covariance matrix. Therefore, it may vary from one time step to another. To determine the smoothing factor, a trade-off curve is widely used, which shows the relation between the sum of squares of the residuals and Laplacian of the slip model [e.g., *Jónsson et al.*, 2002]. This approach is implemented manually (or semi-manually using finite difference methods [*Hearn and Bürgmann*, 2005]), requiring lots of interaction and thus is not applicable to large time series such as the ones considered here. Other methods include Bayesian inversion that jointly estimates the slip model and the associated smoothing factor [e.g., *Fukuda and Johnson*, 2008] and the generalized cross-validation (GCV) [e.g., *Golub et al.*, 1979; *Wahba*, 1977] that minimizes the weighted sum of squares of the residuals divided by a quantity containing the trace of the inverse of the design matrix. The GCV method can be implemented automatically through optimization. However, in many cases, including our study, the GCV function becomes very flat in the vicinity of the optimum value and thus estimating the proper smoothing factor is not possible. To devise an automatic approach for estimating the optimum smoothing factor, we present the following procedure, which simply uses the trade-off curve. As seen in Figure (2), the optimum smoothing factor is obtained at the location of the maximum curvature or minimum curvature radius (i.e., the radius of the tangent circle to the curve). Assuming functions $\Gamma(\gamma) = \|z_t(\gamma)\|$ and $\Pi(\gamma) = \|D\mu_t(\gamma)\|$, (the parameters are described in section 2.2 and $\| \|$ is the norm operator) the curvature (Θ) of the curve $T(\gamma) = (\Pi(\gamma), \Gamma(\gamma))$ is obtained as follows [e.g., *Langevin*, 2001]:

$$\Theta(\gamma) = \frac{\dot{\Pi}\ddot{\Gamma} - \ddot{\Pi}\dot{\Gamma}}{\left(\dot{\Pi}^2 + \dot{\Gamma}^2\right)^{3/2}} \quad (19)$$

[18] Dotted values represent the partial derivative with respect to γ and the curvature radius is defined as the inverse of $\Theta(\gamma)$. The optimum smoothing factor can be obtained by maximizing $\Theta(\gamma)$ through a nonlinear optimization method such as Monte Carlo search approaches (more details on Monte Carlo search approaches are provided in *Shirzaei and Walter* [2009]).

2.4. Estimating the Relative Weight of Various Observations

[19] Often in geophysical optimization problems, we deal with more than one dataset, each of which includes different numbers of observations with variable uncertainties. The formal error (i.e., the standard deviation) of each observation can be obtained using the nominal error of the measuring tools [e.g., *Mikhail*, 1976]. Nonetheless, we often find that the relative weights obtained from direct consideration of the data and their formal uncertainties does not result in an optimal and balanced consideration of constraints from diverse types of data. The issue of estimating the relative weights is crucial as it accounts for the inconsistency among different observations, due to scaling, systematic errors, and so forth. To address this issue, we adapt a method initially proposed for combining various space-borne and terrestrial data sets to model the earth's gravity field [*Koch and Kusche*, 2002]. Given the observation sets τ_1 (InSAR data) and τ_2 (creep data) with covariance matrices of $\Sigma_{\tau_1 \tau_1}$ and $\Sigma_{\tau_2 \tau_2}$ that are related to the model parameters μ (fault slip) through design matrices B_1 and B_2, the system of equations in matrix form is as follows:

$$\begin{pmatrix} \tau_1 \\ \tau_2 \end{pmatrix} + \begin{pmatrix} z_1 \\ z_2 \end{pmatrix} = \begin{pmatrix} B_1 \\ B_2 \end{pmatrix} \mu \quad , \quad P = \begin{pmatrix} S_{0_1}^2 \Sigma_{\tau_1 \tau_1}^{-1} & 0 \\ 0 & S_{0_2}^2 \Sigma_{\tau_2 \tau_2}^{-1} \end{pmatrix} \quad (20)$$

where z contains the observation residuals (without weighting) and S_0^2 is the secondary variance factor. A least square estimate of the parameters μ (denoted by $\widehat{\mu}$) can be obtained from the following normal equations:

$$\left(B_1^T P_1 B_1 + B_2^T P_2 B_2\right) \widehat{\mu} = \left(B_1^T P_1 \tau_1 + B_2^T P_2 \tau_2\right) \quad (21)$$

By introducing the relative weighting factor $\vartheta = \frac{S_{0_2}^2}{S_{0_1}^2}$, equation (21) is rewritten as

$$\left(B_1^T \Sigma_{\tau_1 \tau_1}^{-1} B_1 + \vartheta B_2^T \Sigma_{\tau_2 \tau_2}^{-1} B_2\right) \widehat{\mu} = \left(B_1^T \Sigma_{\tau_1 \tau_1}^{-1} \tau_1 + \vartheta B_2^T \Sigma_{\tau_2 \tau_2}^{-1} \tau_2\right) \quad (22)$$

[20] The updated variance factor and relative weighting factor are expressed as

$$\widehat{S}_1^2 = \widehat{z}_1^T P_1 \widehat{z}_1 \Big/ d_{f1}$$

$$\widehat{S}_2^2 = \widehat{z}_2^T P_2 \widehat{z}_2 \Big/ d_{f2}$$

$$\widehat{\vartheta} = \widehat{S}_2^2 \Big/ \widehat{S}_1^2$$

$$\widehat{z}_1 = B_1 \widehat{\mu} - \tau_1$$

$$\widehat{z}_2 = B_2 \widehat{\mu} - \tau_2$$

$$d_{f1} = n_1 - tr\left(B_1^T P_1 B_1 \left(B_1^T P_1 B_1 + B_2^T P_2 B_2\right)^{-1}\right)$$

$$d_{f2} = n_2 - tr\left(B_2^T P_2 B_2 \left(B_1^T P_1 B_1 + B_2^Y P_2 B_2\right)^{-1}\right) \quad (23)$$

where tr is the trace operator and n_1 and n_2 are length of τ_1 and τ_2, respectively. Starting from $\vartheta = 1$, the optimum relative
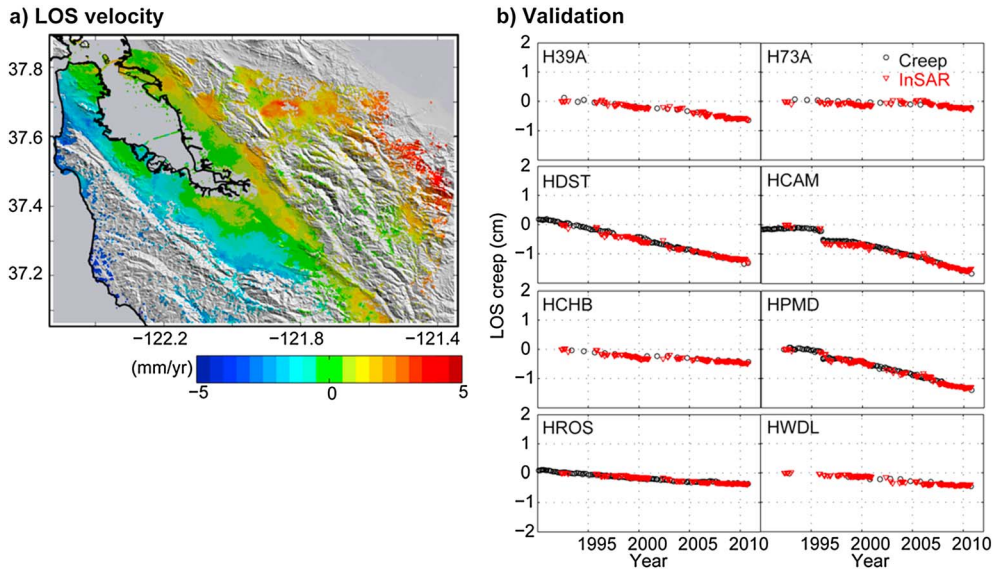
Figure 3. (a) The LOS velocity from 1992–2010 InSAR time series before removing the regional trend. Red and blue colors indicate movement toward and away from the satellite, respectively. The satellite incidence angle and heading angles are 23° and 188°. (b) Comparison of InSAR time series (red triangles) versus surface creep measurements (black circles) at eight stations. The locations are shown in Figure 1 and the statistical comparison is provided in Table 1.

weight can be obtained through iterations. The stopping criterion is $|\vartheta_k - \vartheta_{k-1}| < \varepsilon$, where ε is a small number (e.g., 10^{-3}).

3. Results: InSAR Time Series and Validation

[21] The SAR data set includes 52 and 50 acquisitions of the ERS1/2 and Envisat satellites, respectively, which were collected in beam mode I2 along the descending orbit track 70 and span the period from 1992 to 2010. Given this data set, we generated 401 ERS and 430 Envisat interferograms, respectively, with perpendicular and temporal baselines smaller than 400 m and 4 years (see Figure A1 for baseline plots). The pixel size is 80 m × 80 m equivalent to multilooking factor of 4 × 20 in range and azimuth, respectively. The geometrical phase is estimated and subtracted using satellite precise ephemeris data and a reference Shuttle Radar Topography Mission digital elevation model of 90 m resolution [*Franceschetti and Lanari*, 1999]. Following section 2.1, we generate the InSAR time series of the surface displacement. Note that the analysis is limited to the areas where the ERS and Envisat data overlap. Thus, the area of coverage is slightly smaller than what could be obtained by analyzing only ERS or Envisat data. The useful data points are limited to the urban area and where the surface terrain is stable over the 18 years observation (Figure 3a). It is noteworthy that the number of stable data points decreases with the length of the observation period, i.e., the longer the time series is the fewer stable pixels are identified. Despite this limitation, our proposed method for identifying stable pixels could identify more than 350,000 elite pixels, which is comparable with earlier works that dealt with a shorter observation period [e.g., *Lanari et al.*, 2007; *Shanker et al.*, 2011].

[22] Figure 3a shows a map of the LOS velocities of the obtained InSAR time series. We also identified a few pixels inside the San Francisco Bay, some of which are associated with exposed rocks and built structures. Major components

of the resolved signal include displacement due to plate motions and elastic strain accumulation across the San Andreas Fault system, as well as non-tectonic land subsidence and rebound. Here, we focus on the discontinuity along the Hayward fault that is an indicator for shallow fault creep and comprises shorter wavelength features compared to the long-term interseismic deformation components [e.g., *Schmidt et al.*, 2005].

[23] In the following, the regional trend of the displacement field due to steady plate-boundary deformation is simulated and subtracted using a model of 14 deep dislocations whose slip rates are constrained by GPS data (Table A1; see also Table DR1 in *Bürgmann et al.*, [2006]). Figures A5 and A6 show the LOS velocity field corrected for regional interseismic shearing and the interseismic model correction, respectively. We note that InSAR data with long wavelength orbit and atmospheric artifacts are not well suited to evaluate long wavelength signals such as that of the elastic strain field due to deep slip spread out laterally over several locking depths.

[24] Before using this data set to model the time-dependent creep on the Hayward fault, we validate the InSAR time series against the surface creep data. Surface creep rates are obtained from alignment array measurements [*Lienkaemper et al.*, 1991; *Lienkaemper and Galehouse*, 1997b] and creepmeter data [*Bilham and Whitehead*, 1997] along the Hayward fault (see Figure 1). These data indicate creep rates of up to ~9 mm/yr along a ~4 km section near the south end of the creeping HF (km 63–67), while the creep rate along the rest of the fault ranges from 3–4 mm/yr in Oakland (km 20–27) to 4–6 mm/yr elsewhere [*Lienkaemper et al.*, 2012]. *Lienkaemper et al.* [2012] document changes in creep rate associated with the apparent effects of the 1989 Loma Prieta earthquake and several slow-slip transients. For example, at station HCAM, a step in both surface creep and InSAR time series is evident, which is associated with 9 February 1996 creep event [*Lienkaemper et al.*, 1997]. The

Table 1. The Statistical Comparison of the InSAR Time Series Versus Surface Creep Data Obtained by Alignment Stations[a]

No	Station	Distance from Pt. Pinole (km)	InSAR-creep rate (mm/yr)	Alignment creep rate (mm/yr)	TS. Std.[b] (InSAR-Creep) [mm]	LOS Vel. Diff[c] (InSAR-Creep) [mm/yr]
1	HLSA	23	5.2	4.4	0.9	0.2
2	HLNC	25	3.8	3.9	0.4	0.03
3	H39A	27	3.7	4.2	0.9	0.1
4	H73A	30	1.7	3.3	0.8	0.5
5	HENC	32	1.9	2.9	1	0.3
6	HCHB	35	3.9	4.2	0.3	0.05
7	H167	40	5.9	5.1	1.1	0.2
8	HROS	42	4.2	4.3	0.3	0.03
9	HDST	43	6.4	4.6	0.7	0.05
10	HPAL	45	4.4	4.6	0.3	0.03
11	HSEP	47	4.6	5.7	0.4	0.3
12	HWDL	49	5.4	4.5	0.5	0.3
13	HAPP	54	7.1	5.6	0.8	0.5
14	HHAN	61	5.5	5.9	1.2	0.1
15	HRKT	61	5.7	5.4	1	0.1
16	HUNI	62	7.8	6.6	1	0.2
17	HPIN	64	6.7	6.6	1	0.03
18	HCAM	65	4.0	4.4	0.8	0.1
19	HPMD	65	6.0	5.9	0.6	0.03

[a]The creep data are projected into the LOS of the satellite (incidence angle = 23°, heading angle = 188°, and Hayward fault strike 145°).
[b]TS. STD. = LOS displacement time series standard deviation.
[c]LOS velocity difference is provided to enable a comparison with earlier studies such as *Shanker et al.* [2011].

kinematic model of this event is further investigated in section 4.2. Figure 3b and Table 1 show the results of comparing the InSAR time series against the surface creep observations. The horizontal creep data are projected onto the LOS of the satellite (given incidence angle = 23°, heading angle = 188°, and average fault azimuth of 145°). Despite the low amplitude of the creep, a very good agreement between InSAR and creep time series is evident. The standard deviation of the difference between these data sets along the Hayward fault is ~1 mm for the creep time series and ~0.1 mm/yr for the estimated LOS velocity.

4. Results: Fault Slip Model

[25] To investigate spatial and temporal variations of creep on the Hayward fault, we employ a time-dependent modeling scheme and jointly invert the InSAR and surface creep time series (see section 2.2). As described above, the InSAR data were previously corrected for regional interseismic deformation. We also remove the annual component of the measured InSAR surface displacement that is mostly due to non-tectonic signals such as discharge/recharge of aquifers (Figure A2). Figure A2.a suggests modest perturbation by hydrological processes along the Hayward fault except for an area near the southernmost extent of the creeping surface trace. Figure A2.b also presents the phase of the corrected seasonal component that highlights the areas perturbed synchronously. We downsample the InSAR data set using the approach suggested by *Schmidt et al.* [2005], where a uniform downsampling scheme is implemented at two different resolutions. The near field (20 km adjacent to the fault) is subsampled at the resolution of 100 m, while the rest of the data set is reduced to 500 m pixel spacing, which provides ~2500 data points used for the inversion.

[26] The next stage is to estimate the relative weight of the InSAR and surface creep data (see section 2.4). Due to time variability of the observation noise, the best approach is to estimate the relative weight for every time step. However,

to reduce the computation time, we only estimate the relative weight of the creep velocity versus the InSAR deformation velocity and assumed the same relation exists for every time step of the displacement time series. The estimated relative weight of the creep data is 5.33 times that of InSAR data.

4.1. Time-Dependent Creep Model

[27] Time-dependent creep modeling comprises two steps of static inversion and temporal filtering that are implemented in an iterative manner [*Shirzaei and Walter*, 2010]. As detailed in section 2.2, the static inversion includes the joint inversion of the InSAR and surface creep data using an iterative L2-norm optimization approach that reduces the effects of outliers on the model parameters. The Hayward fault geometry is the best fitting surface through the relocated microseismicity along the fault (provided by R. Simpson, pers. comm., 2008). Therefore, the geometry of the fault is constant throughout the inversion, which reduces the problem to a linear optimization. Although we attempt to remove the regional deformation field and the effect of orbital errors in each interferogram, to account for the residuals of these effects and the potential phase offset due to an unstable reference point, we consider an unknown ramp and an offset term for every time step, which are estimated jointly with the distribution of the fault creep. The only constraint we apply is on the sense of slip, for which we only allow for right-lateral strike slip. Given the complexity of the fault plane geometry (Figure 4), we employ a mesh of triangular dislocations [*Meade*, 2007] to represent the geometry of the Hayward fault. At every time step in the distributed slip inversion, a smoothing factor is estimated using the method explained in section 2.3. Figure (A3) shows the estimated smoothing factor for every time step. Following static inversion, we obtain the distributed slip for each time step and the associated variance-covariance matrix, which is optimized through reweighted L2-norm minimization. These parameters form the input to the second stage, which is the temporal filtering using the Kalman filter [*Shirzaei and Walter*, 2010].
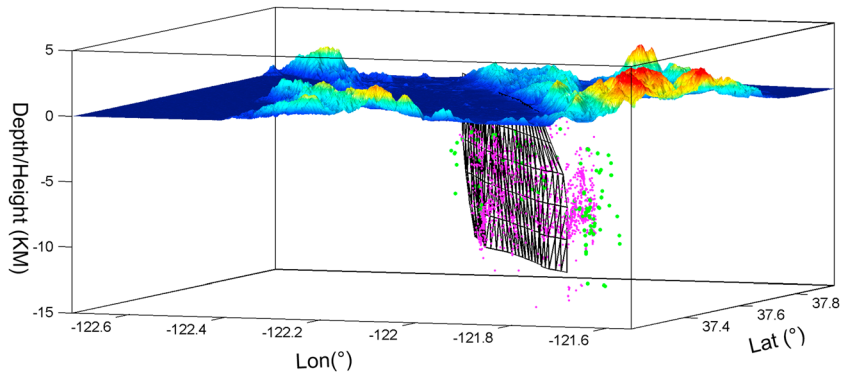
Figure 4. Hayward fault geometry and the 3-D mesh of the surface topography. The purple dots present micro seismicity for the period 1992–2010 (courtesy http://www.ldeo.columbia.edu/~felixw) and the green dots are repeating earthquakes (provided by T. Taria, pers. comm., 2008).

As detailed in section 2.2 and broadly discussed in [*Shirzaei and Walter*, 2010], the LKF is used to reduce temporal noise and update the variance-covariance matrix of the distributed slip. Since the results of the LKF may not fully reproduce the observations (i.e., the model is not optimal in terms of spatial mean square error), we repeat the static inversion with the initial creep values set to equal those obtained from the LKF of the previous iteration. Each iteration of the time-dependent modeling includes a static inversion followed by temporal Kalman filtering. This procedure continues until reaching some stopping criteria, in this case the difference between models obtained from the LKF and static inversions becoming smaller than ε (here, 1 mm). Here, after 10 iterations the stopping criterion was reached.

[28] The final time-dependent creep model of the Hayward fault for 1992–2010 is shown in Figures 5a and 5b and in the animation in the electronic supplement. The darker colors indicate more right-lateral creep. Figure A4 also demonstrates the model resolution in terms of standard deviation of the resolved creep. The resolution test suggests that along the shallow segments of the Hayward (except the northernmost portion), creep features of 0.5 mm or even smaller can be resolved. In contrast, at the base of the fault, the creep resolution drops to 2 mm and worse, which likely is an overestimation of the true resolution due to the smoothing operator. In Figure 5a, the linear velocity obtained from our time-dependent creep modeling and the location of the creepmeters and alignment arrays and their associated observations of actual surface creep are shown for comparison with the creep rate model. There is very good agreement between the model and surface creep observations. Figure 5b also shows examples of creep time series at several points on the Hayward fault interface, which demonstrates nonlinear behavior at various places. Our results show that the upper 3–4 km of the Hayward from 45 to 70 km distance creep faster than the northern section (km 0–30). In the north, the faster creep occurs at depth of 5–10 km. A large locked patch that creeps at <1 mm/yr is constrained at km 25–45, in agreement with earlier works [*Funning et al.*, 2005; *Malservisi et al.*, 2003; *Schmidt et al.*, 2005; *Simpson et al.*, 2001] but not with the model result of *Evans et al.* [2012]. The area of modeled subsurface creep correlates well with the distribution of repeating micro-earthquakes

(magenta circles in Figure 5a), which are inferred to be driven to fail frequently by the surrounding fault creep [e.g., *Nadeau and Mcevilly*, 2004; *Schmidt et al.*, 2005]. Repeating earthquakes are nearly absent in the inferred low-slip zones. The major locked zone is most likely the location of future large events and ruptured in the 1868 ~Mw6.8 southern Hayward earthquake. We also infer several smaller, low-slip zones including one south of Berkeley (km 15–20) and another near km 55–65. These low-slip patches may contain small, locked asperities that may rupture during smaller events or, in the worst case scenario, rupture together with the big locked patch to generate a bigger earthquake.

[29] Figure 5c shows the time series of the spatial root mean square (RMS) of the mismatch between observed and modeled surface deformation. The maximum RMS for the InSAR and surface creep data is less than 5 mm and 1 mm, respectively. The spatial distribution of the residuals (observed—modeled linear LOS and surface creep velocity) for the creep rate model is shown in Figures 5d and A8. Both measures of misfit show a good agreement between model and data. Figure A7 also presents the modeled LOS velocity field.

4.2. Kinematic Source Model of Creep Events

[30] On 17 October 1989, the Mw 6.9 Loma Prieta earthquake reduced surface creep rates along the southern Hayward fault caused by a reduction of right-lateral shear stress in the event [*Lienkaemper et al.*, 1997]. Following this earthquake, the southernmost segment of the Hayward fault stopped creeping for about 6 years and the quiescence was ended by a rapid creep event of 25–30 mm displacement and slow recovery. Creep is only now reaching the pre-Loma Prieta event rate [*Lienkaemper et al.*, 2012]. Using a spring-slider model with a rate- and state- dependent friction law, *Schmidt and Bürgmann* [2008] investigated the general pattern of the ~6 years quiescence and the creep event following the Loma Prieta earthquake. *Kanu and Johnson* [2011] used similar spring-slider models combined with a boundary element model and suggest that the creep event extended to a depth of ~4–7.5 km. However, a kinematic model of this creep event constrained by deformation data remains to be resolved.

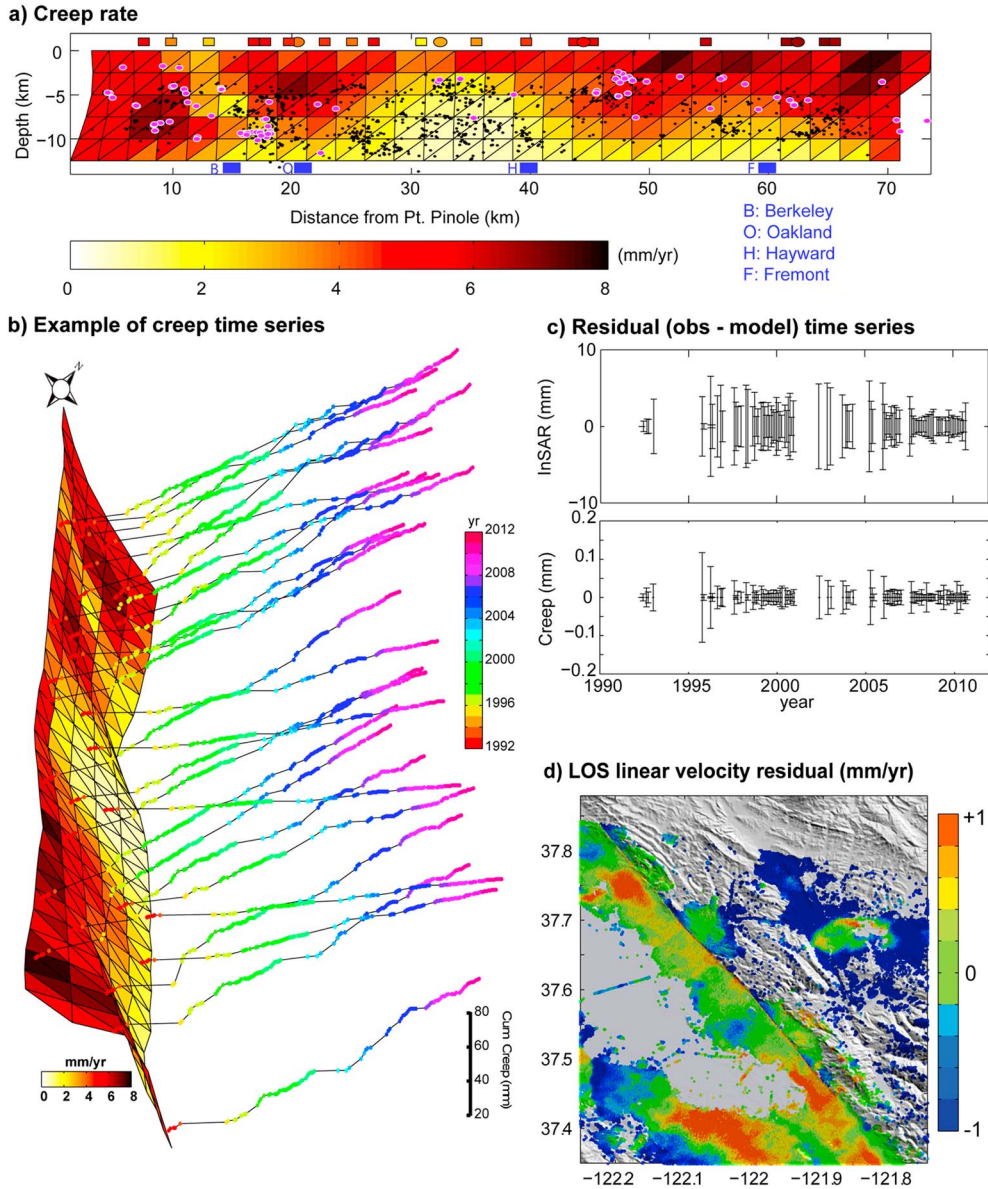[31] The advantage of our time-dependent model is the ability of constraining the long-term as well as transient

Figure 5. (a) Average right-lateral creep rate along the Hayward fault. The black dots are microseismicity along the fault (courtesy http://www.ldeo.columbia.edu/~felixw). The magenta circles show the location of repeating events. Average 1992–2010 rates from surface measurements are shown by symbols on top with same color scale. Squares represent 19 alignment stations and circles are four creepmeters. (b) 3-D perspective of the Hayward fault creep rate and examples of creep time series associated with various patches along the fault. (c) Time series of the root mean square error (RMS) for the InSAR and creep data (observed-modeled). (d) The close up view of the spatial distribution of the residuals between the Hayward fault creep rate model and the LOS linear velocity of the surface deformation (observed-predicted average LOS velocity).

components of creep on the Hayward fault. Thus, despite an interruption of the ERS SAR acquisitions from 1993 to 1995, the kinematic model of the February 1996 creep event is embedded in our time-dependent model. To obtain this model, we subtract the model associated with the time step before the event from that after the event (i.e., the creep during the period 10 November 1995–29 March 1996). The result of this calculation is shown in Figure 6a. The source of the creep event is constrained as an area of high slip extending 8 km along the southern part of the Hayward fault

and to 7 km depth, consistent with the depth extent proposed by *Kanu and Johnson* [2011] based on constraints provided by the frictional response of the fault. The field observations of surface creep obtained from alignment array and creepmeter stations during this time are shown on top of the creep model and demonstrate a good agreement between the data and model.

[32] *Lienkaemper et al.* [2012] suggest that following an Mw 4.2 earthquake on 20 July 2007, in Oakland near km 26.4 and at a depth of 4.1 km, a modest (~10–20 mm)
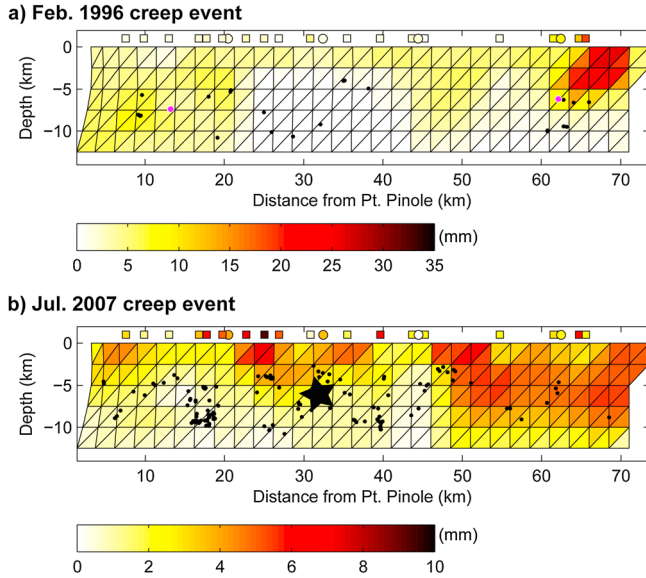
a) Feb. 1996 creep event

b) Jul. 2007 creep event

Figure 6. (a) Source model of the February 1996 creep event (slip from 10 November 1995 to 29 March 1996). (b) Source model of the July 2007 creep event (slip from 23 December 2006 to 25 August 2007). The 20 July 2007 $M_w = 4.2$ event is shown by a black star. The field measurements of surface creep spanning the respective time periods are shown above the model. Black dots show background seismicity and magenta circles are repeating events that occurred during the two time intervals.

creep event initiated at km ~20 to ~34. To investigate the source of this event, we subtract the source model obtained for time step 23 December 2006 from that of 25 August 2007 (Figure 6b). Despite apparent uncertainty of the surface creep observations for this period (note the fluctuation of the surface creep data along the fault) and a relatively large gap in the InSAR time series, a substantial creep increment of up to 10 mm is revealed at km 22–37 and ~5 km deep. However, due to data uncertainty caused in part by the relatively long gap in the InSAR time series and the modest amplitude of the inferred creep, the source model for the July 2007 creep is not as well constrained as that of February 1996.

[33] To identify any other accelerated slow slip transients that are not evident in the surface creep data, we calculate the acceleration of the creep for every patch on the fault interface for the period 1992–2010 using a cubic polynomial fit (see also Figure 5b for examples of fault patch creep time series). Figure 7a shows the distribution of the creep acceleration. The area of the February 1996 aseismic slip transient shows a significant negative acceleration as the large-amplitude creep event occurred early in the time series. To the north, near km 20–30, there is an area of a large positive acceleration. Plotting time series of the average creep of this area (Figure 7b) shows that in February 1996 and after ~6 years of no creep, a period of elevated creep started. This could be an indicator of another slow-slip transient that initiated close in time to that on the southern segment. Since this accelerated creep is right next to the major locked segment of the Hayward fault, understanding the effect of time-dependent creep on the loading of the locked rupture asperity is of importance.

5. Discussion

[34] We document time-dependent creep along the Hayward fault and provide the spatiotemporal history of the aseismic slip (see Figure 5). Although there is no other study to confirm temporal aspects of the modeled subsurface creep rate variations, the obtained kinematic model of the creep rate (Figures 5a and 5b) and creep events (Figure 6) is consistent with earlier studies [e.g., *Bürgmann et al.*, 2000; *Gans et al.*, 2003; *Kanu and Johnson*, 2011; *Lienkaemper et al.*, 2012; *Malservisi et al.*, 2003; *Schmidt et al.*, 2005; *Simpson et al.*, 2001; *Wyss*, 2001].

[35] Aseismically slipping faults, such as the central San Andreas, the Calaveras and the Hayward faults tend to be well illuminated by highly localized seismicity, including repeating events on the fault plane [e.g., *Nadeau and Mcevilly*, 1999; *Schaff et al.*, 2002; *Waldhauser and Ellsworth*, 2002]. We infer a large patch of low model creep (<1 mm/yr) (km 25–45) as a locked zone, which is devoid of repeating earthquakes (see Figure 5). However, as seen in the fault plane view (Figure 8), a large number of micro-earthquakes occur in this area, which may appear to contradict the model results suggesting this area is locked. Consideration of the 3-D distribution of the seismicity reveals that the area of the locked patches correlates with broadly distributed seismicity adjacent to the fault, whereas seismicity along the fast creeping segments is closely aligned with the fault trace (Figure 8; see also *Gans et al.*, [2003]). The average distance of the microseismicity from the fault can be considered as an indirect indicator marking creeping and locked segments of the fault, where along the creeping segments the seismicity is highly localized near the fault interface.

[36] Given a long-term slip rate of ~9 mm/yr [e.g., *Lienkaemper et al.*, 1991], we estimate the slip deficit accumulating along the Hayward fault (Figure 9a). Figure 9a shows that a maximum deficit of 1.5 m accumulated along km 25–45 consistent with the slip inferred for the 1868 event [*Yu and Segall*, 1996]. When computing this seismic potential and stress build up since the 1868 earthquake, we

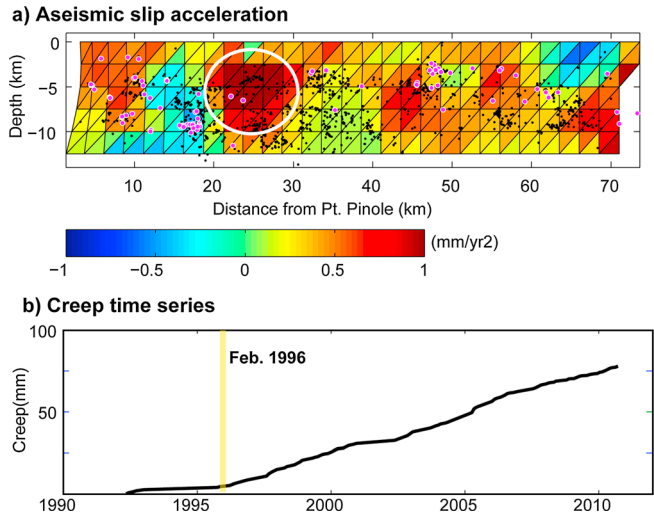**a) Aseismic slip acceleration**

b) Creep time series

Figure 7. (a) Distribution of the creep acceleration along the Hayward fault. The area of the high positive acceleration is marked with a white circle. (b) Time series of creep for the average of the patches inside the circled area in Figure 7a.
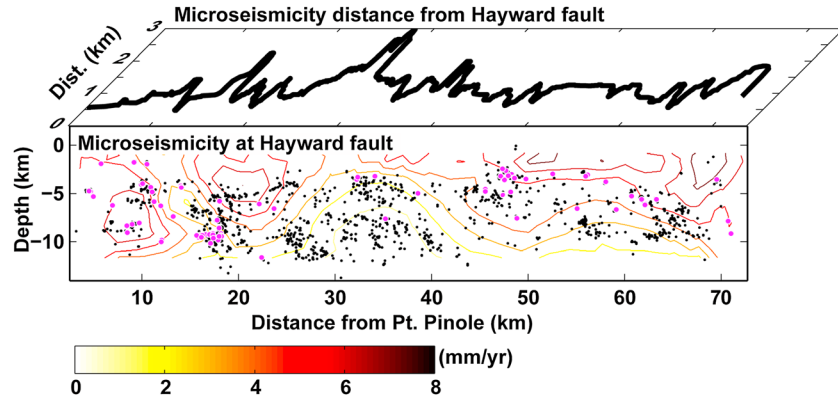
Figure 8. The distribution of microseismicity within 2 km from fault surface (black dots; courtesy http://www.ldeo.columbia.edu/~felixw) and repeating earthquakes (purple circles; *T. Taira* pers. comm. [2011]). Contours show the average creep rate on the Hayward. The top row shows the average distance of the microseismicity from the fault.

assume that the pattern and average rate of slip deficit accumulation have been stable, since soon after the earthquake. While repeat measurements of offset cultural features crossing the fault suggest that time-averaged creep rates have remained constant for much of the twentieth century [e.g., *Lienkaemper and Galehouse*, 1997a; *Schmidt and Bürgmann*, 2008], substantial slip rate variations may well have occurred during the last 140 years. The potential size of the next major seismic event varies from Mw ~6.3 to Mw ~6.8, depending on if only the major central locked patch ruptures or the rupture propagates through the entire 70 km of the Hayward fault including the areas of low slip deficit. A Mw ~7.0 would be expected if the Hayward Fault were fully locked. An even worse scenario would include rupture propagating southward through the Mission Hills section to the Calaveras fault and northward across San Pablo Bay and along the adjoining Rodgers Creek fault. Transient creep events near the major central locked patch such as the one shown in Figure 7, may temporarily increase the probability of a large earthquake on the Hayward fault as has been suggested for Cascadia [*Mazzotti and Adams*, 2004].

[37] To investigate the effect of Hayward fault creep on the locked portions of the fault in terms of stress transfer, we calculate the Coulomb failure stress change induced by fault creep [*King et al.*, 1994]. The Coulomb stress change is defined as $\Delta CFS = N_s + f_c S_s$, where S_s is the shear stress change on the fault (positive in the inferred direction of slip), N_s is the normal stress (positive for unclamping), and f_c is the effective friction coefficient (here assumed equal to 0.4). We examine the degree to which creep on the Hayward fault enhances loading on the locked asperities along the fault. Figure 9b shows the rate of Coulomb stress change imparted from the creep rate distribution estimated on the Hayward fault. There are two major areas that receive significant positive stress change, including the inferred locked patch (km 25–45) with a mean stress change rate of 0.003 MPa/yr. The other area that experiences significant positive stress changes is at km 10–20, south of Berkeley. Except for these two areas, the creep reduces the accumulated stress on most of the Hayward fault. The cumulative Coulomb failure stress change from creep since the 1868 earthquake on the central and northern locked zones amounts to ~0.5 MPa. This stress

is in addition to the background stressing rate due to tectonic plate motions which depending on the distribution of lower crustal deformation is estimated at 0.01–0.015 MPa/yr [*Parsons*, 2002].

[38] The creeping behavior of the Hayward fault varies with time and along the fault. This variable behavior may be determined by variations in the stiffness of the surrounding rocks, the frictional properties of the fault interface, and stress interaction with neighboring fault systems or other time-dependent loads [*Lienkaemper et al.*, 1997; *Logan*, 1978; *Marone et al.*, 1990; *Marone and Scholz*, 1988; *Schmidt and Bürgmann*, 2008]. The aseismic slip significantly loads the locked zones and thus increases the seismic hazard. Therefore, the spatiotemporal variability of the creep leads to a time-variable seismic hazard that suggests further
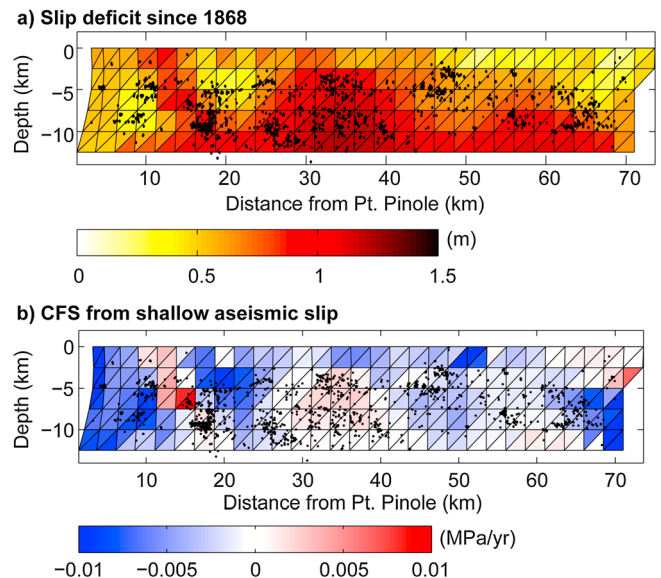

Figure 9. (a) Slip deficit since the last major seismic event in 1868 by assuming a long-term slip rate of ~9 mm/yr [e.g., *Lienkaemper et al.*, 1991]. (b) Average rate of Coulomb failure stress change along the Hayward fault imparted by aseismic creep from 1992 to 2010.

research on developing time-dependent hazard models to provide an updated estimate of earthquake probability by taking into account all time-dependent and independent factors. Slow slip transients on the creeping portions of the fault and associated increases in seismicity rates reflect short-term increases in earthquake hazard that may be relevant for operational earthquake forecasting efforts [e.g., *Jordan et al.*, 2011; *Mazzotti and Adams*, 2004].

6. Conclusion

[39] We present a spatiotemporal model of creep on the Hayward fault. To this end, we explored an 18-year long time series of InSAR deformation and surface creep data. Our time-dependent creep model reveals a persistent accumulation of slip deficit (more than 90% of the geologic slip rate) along buried ~25-km long and ~7-km wide section of the fault. Our model also identifies several other smaller locked patches. Our results suggest that the creep rate is faster at shallow depths along the southern Hayward fault compared with the northern fault section, which has higher rates at depth. This variation may reflect changes in the regional stress field and/or material heterogeneities along the Hayward fault.

[40] We find that in addition to the background stressing rate, the fault creep is loading the major locked asperity of the Hayward fault at a mean rate of ~0.003 MPa/yr. This indicates the direct impact of fault creep on the adjacent locked segments and the size and recurrence interval of large seismic events. Given that the Hayward fault accumulates a slip deficit of 30–90% of its long-term slip budget along the 70-km long section of the fault zone we considered, we estimate the accumulated seismic moment since the last big event in 1868 to be capable of producing an Mw ~6.3–6.8, today.

[41] As a byproduct of our time-dependent creep model, we constrained kinematic models of the February 1996 and July 2007 shallow creep events. Moreover, we identified a deeper accelerated creep transient that occurred to the NW of the major locked patch, starting early in 1996. As this primary locked zone is the potential nucleation site for a future large event, understanding its relation to the fast creeping segments is of importance. Slow slip transients on the creeping portions of the fault and associated increases in seismicity rates reflect short-term increase in stressing rates and thus earthquake hazard.

Notation

N	Number of images minus 1
φ_z	Observed interferometric phase in real domain
φ_x	True interferometric phase in real domain
r	Additive zero-mean noise in real domain
ρ	Interferometric phase coherence
n	Multilooking factor
$\widehat{r}^c, \widehat{r}^s$	Real and imaginary part of interferometric phase noise in complex domain
k	Number of interferograms
(ζ, η)	Pixel location in range and azimuth direction
σ_c^2, σ_s^2	Real and imaginary part of interferometric phase variance in complex domain
Im, Re	Real and imaginary part of interferometric phase in complex domain
σ^φ	Standard deviation of interferometric phase in real domain
σ	Reference standard deviation of interferometric phase in real domain
∂	Partial derivative
(x,y)	Pixel location in geographic coordinate system
χ^2	Chi-square probability density functions
L_R	Line-of-sight range change in a single interferogram
λ	Radar wavelength
σ_l	Reference standard deviation of observed the LOS range change in a single interferogram
$\delta\phi$	Unwrapped phase of an interferogram converted to displacement
$\hat{\psi}$	Estimated LOS displacement time series
ψ	True LOS displacement time series
A	Design matrix relating unwrapped phase change to unknown LOS displacement
$\varepsilon_{\bar\phi}$	Unwrapped phase error
P	Weighting matrix of observations
T	Tuning factor in re-weighted least squares
Q^i	Updated weighting matrix of unwrapped phase at iteration i
W^i	Down-weighting factor of observation outliers at iteration i
S	Variance factor used in reweighted least square
Σ	Variance-covariance matrix
τ_t	Surface deformation observation at time t
z_t	Observation residual at time t
B	Design matrix at time t relating surface deformation to fault creep (B_1: InSAR, B_2: Creep)
μ_t	Fault slip
lb_t, ub_t	Lower and upper bound of fault creep at time t
S_0^2	Primary variance factor
(θ, β)	Fault patch location along strike and dip
ϑ	Relative weighting factor
γ	Smoothing factor
D	Laplacian operator
H	Observation matrix used in Kalman filter
F_t, G_t	Process and measurement noise used in Kalman filter
Φ	State transition matrix used in Kalman filter
U_t	Measured slip at time t used in Kalman filter t
$\widehat{\mu_t^-}, \widehat{\mu_t^+}$	A priori and posteriori fault slip at time t
P_t^-, P_t^+	A priori and posteriori weighting matrix at time t
Θ	Curvature
ΔCFS	Coulomb failure stress change
S_s	Shear stress
f_c	Effective friction coefficient
N_s	Normal stress

References

Aagaard, B. T., R. W. Graves, D. P. Schwartz, D. A. Ponce, and R. W. Graymer (2010), Ground-motion modeling of Hayward fault scenario earthquakes, part I: Construction of the suite of scenarios, *Bull. Seismol. Soc. Am.*, *100*, doi:10.1785/0120090324.

Amiri-Simkooei, A. (2003), Formulation of L1 norm minimization in Gauss-Markov models, *J. Surv. Eng.*, *129*(1), doi:10.1061/(ASCE)0733-9453.

Bilham, R., and S. Whitehead (1997), Subsurface creep on the Hayward fault, Fremont, California, *Geophys. Res. Lett.*, *24*(11), 1307–1310.

Bjerhammar, A. (1973), *Theory of errors and generalized matrix inverse*, Elsevier publishing company, Amsterdam, pp. 127–128 .

Bürgmann, R., G. Hilley, A. Ferretti, and F. Novali (2006), Resolving vertical tectonics in the San Francisco Bay Area from permanent scatterer InSAR and GPS analysis, *Geology*, *34*, 221–224. doi:10.1130/G22064.1.

Bürgmann, R., D. Schmidt, R. M. Nadeau, E. d'Alessio, E. Fielding, D. Manaker, T. V. McEvilly, and M. H. Murray (2000), Earthquake potential along the northern Hayward fault, California, *Science*, *289*(5482), 1178–1182.

Costantini, M. (1998), A novel phase unwrapping method based on network programming, *IEEE Trans. Geosci. Remote Sens.*, *36*(3), 813–821.

Costantini, M., and P. A. Rosen (1999), A generalized phase unwrapping approach for sparse data, Paper presented at in Proceedings of the IEEE 1999 International Geoscience and Remote Sensing Symposium (IGARSS), Hamburg.

d'Alessio, M. A., I. A. Johanson, R. Bürgmann, D. A. Schmidt, and M. H. Murray (2005), Slicing up the San Francisco Bay Area: Block kinematics and fault slip rates from GPS-derived surface velocities, *J. Geophys. Res. Solid Earth*, *110*, doi:10.1029/2004JB003496.

Evans, E. L., J. P. Loveless, and B. J. Meade (2012), Geodetic constraints on San Francisco Bay Area fault slip rates and potential seismogenic asperities on the partially creeping Hayward fault, *J. Geophys. Res. Solid Earth*, *117*, doi:10.1029/2004JB003496.

Ferretti, A., C. Prati, and F. Rocca (2001), Permanent scatterers in SAR interferometry, *IEEE Trans. Geosci. Remote Sens.*, *39*, 8–20, doi:10.1029/2011JB008398.

Franceschetti, G., and R. Lanari (1999), *Synthetic Aperture Radar Processing*, Library of Congress Cataloging-in-Publication Data, Washington, D.C.

Fukuda, J. i., and K. M. Johnson (2008), A fully Bayesian inversion for spatial distribution of fault slip with objective smoothing, *Bull. Seismol. Soc. Am.*, *98*, 1128–1146.

Funning, G., R. Bürgmann, A. Ferretti, F. Novali, and D. A. Schmidt (2005), Kinematics, asperities and seismic potential of the Hayward fault, California from ERS and RADARSAT PS-InSAR, *EOS, Trans. AGU*, *86*.

Gans, C. R., K. P. Furlong, and R. Malservisi (2003), Fault creep and microseismicity on the Hayward fault, California: Implications for asperity size, *Geophys. Res. Lett.*, *30*(19). doi:10.1029/2003GL017904.

Goldstein, R. M., and C. L. Werner (1998), Radar interferogram filtering for geophysical applications, *Geophys. Res. Lett.*, *25*(21), 4035–4038.

Golub, G. H., M. Heath, and G. Wahba (1979), Generalized cross-validation as a method for choosing a good ridge parameter, *Technometrics*, *21*(2), 215–223.

Goswami, J. C., and A. K. Chan (1999), *Fundamentals of Wavelets: Theory, Algorithms, and Applications*, 324 pp., Wiley-Interscience, New York.

Grewal, M. S., and A. P. Andrews (2001), *Kalman Filtering: Theory and Practice Using MATLAB*, 416 pp., Wiley-Interscience, New York.

Han, M., Y. Liu, J. Xi, and W. Guo (2007), Noise smoothing for nonlinear time series using wavelet soft threshold, *IEEE Signal Proc. Lett.*, *14*, 62–65.

Hearn, E. H., and R. Bürgmann (2005), The effect of elastic layering on inversions of GPS data for coseismic slip and resulting stress changes: Strike-slip earthquakes, *Bull. Seismol. Soc. Am.*, *95*, 1637–1653. doi:10.1785/0120040158.

Holland, P. W., and R. E. Welsch (1977), Robust regression using iteratively reweighted least-squares, *Commun. Stat. A-Theor.*, *A6*, 813–827.

Huber, P. J. (1981), *Robust Statistics*, 320 pp., Wiley, New York.

Jónsson, S., H. Zebker, P. Segall, and F. Amelung (2002), Fault slip distribution of the 1999 Mw7.1 Hector Mine Earthquake, California, estimated from satellite radar and GPS measurements, *Bull. Seismol. Soc. Am.*, *92*, 1377–1389.

Jordan, T. H., Y.-T. Chen, P. Gasparini, R. Madariaga, I. Main, W. Marzocchi, G. Papadopoulos, G. Sobolev, K. Yamaoka, and J. Zschau (2011), Operational earthquake forecasting: State of knowledge and guidelines for utilization, *Ann. Geophys.*, *54*(4), doi:10.4401/ag-5350.

Kanu, C., and K. Johnson (2011), Arrest and recovery of frictional creep on the southern Hayward fault triggered by the 1989 Loma Prieta, California, earthquake and implications for future earthquakes, *J. Geophys. Res. Solid Earth*, *116*, doi:10.1029/2010JB007927.

King, G. C. P., R. S. Stein, and J. Lin (1994), Static stress changes and the triggering of earthquakes, *Bull. Seismol. Soc. Am.*, *84*, 935–953, doi:10.1029/2010JB007927.

Koch, K. R., and J. Kusche (2002), Regularization of geopotential determination from satellite data by variance components, *J. Geod.*, *76*(5), 259–268.

Lanari, R., F. Casu, M. Manzo, and P. Lundgren (2007), Application of the SBAS-DInSAR technique to fault creep: A case study of the Hayward fault, California, *Remote Sens. Environ.*, *109*, doi:10.1016/j.rse.2006.12.003.

Langevin, R. (2001), Differential geometry of curves and surfaces, *An Introduction to the Geometry and Topology of Fluid Flows. Proceedings of the NATO Advanced Study Institute*.

Lauknes, T. R., H. A. Zebker, and Y. Larsen (2011), InSAR deformation time series using an L-1-norm small-baseline approach, *IEEE Trans. Geosci. Remote Sens.*, *49*, doi:10.1109/TGRS.2010.2051951.

Lee, J. S., K. P. Papathanassiou, T. L. Ainsworth, M. R. Grunes, and A. Reigber (1998), A new technique for noise filtering of SAR interferometric phase images, *IEEE Trans. Geosci. Remote Sens.*, *36*(5), 1456–1465.

Lienkaemper, J. J., G. Borchardt, and M. Lisowski (1991), Historic creep rate and potential for seismic slip along the Hayward Fault, California, *J. Geophys. Res.*, *96*, 18261–18283.

Lienkaemper, J. J., and J. Galehouse (1998), New evidence doubles the seismic potential of the Hayward fault, *Seismol. Res. Lett*, *69*, 519–523.

Lienkaemper, J. J., and J. S. Galehouse (1997a), Revised long-term creep rates on the Hayward fault, Alameda and Contra Costa counties, California, *Rep.*, pp. 97–690, U. S. Geol. Surv. Open File Rep.

Lienkaemper, J. J., and J. S. Galehouse (1997b), Revised long-term creep rates on the Hayward fault, Alameda and Contra Costa counties, California, *Rep.*, Open-File Rept. 97–690, 618 pp., U.S. Geol. Surv.

Lienkaemper, J. J., J. S. Galehouse, and R. W. Simpson (1997), Creep response of the Hayward fault to stress changes caused by the Loma Prieta earthquake, *Science*, *276*(5321), 2014–2016.

Lienkaemper, J. J., F. S. McFarland, R. W. Simpson, R. G. Bilham, D. A. Ponce, J. J. Boatwright, and S. J. Caskey (2012), Long-term creep rates on the Hayward fault: Evidence for controls on the size and frequency of large earthquakes, *Bull. Seismol. Soc. Am.*, *102*, doi:10.1785/0120110033.

Lienkaemper, J. J., P. L. Williams, and T. P. Guilderson (2010), Evidence for a twelfth large earthquake on the southern Hayward fault in the past 1900 years, *Bull. Seismol. Soc. Am.*, *100*, doi:10.1785/0120090129.

Logan, J. M. (1978), Creep, stable sliding, and premonitory slip, *Pageoph*, *116*, 773–789.

Lopez-Martinez, C., and X. Fabregas (2002), Modeling and reduction of SAR interferometric phase noise in the wavelet domain, *IEEE Trans. Geosci. Remote Sens.*, *40*(12), 2553–2566.

Malservisi, R., C. Gans, and K. P. Furlong (2003), Numerical modeling of strike-slip creeping faults and implications for the Hayward fault, California, *Tectonophysics*, *361*(1–2), doi:10.1016/S0040-1951(02)00587-5.

Marone, C., C. B. Raleigh, and C. H. Scholz (1990), Frictional behavior and constitutive modeling of simulated fault gouge, *J. Geophys. Res.*, *95*, 7007–7025.

Marone, C., and C. H. Scholz (1988), The depth of seismic faulting and the upper transition from stable to unstable slip regimes, *Geophys. Res. Lett.*, *15*, 621–624.

Marshall, J., and J. Bethel (1996), Basic concepts of L1 norm minimization for surveying applications, *J. Surv. Eng.*, *122*(4), 168–179.

Mazzotti, S., and J. Adams (2004), Variability of near-term probability for the next great earthquake on the Cascadia subduction zone, *Bull. Seism. Soc. Am.*, *94*, doi:10.1785/012004032.

Meade, B. J. (2007), Algorithms for the calculation of exact displacements, strains, and stresses for triangular dislocation elements in a uniform elastic half space, *Comput. Geosci.*, *33*, doi:10.1016/j.cageo.2006.12.003.

Mikhail, E. M. (1976), *Observations and Least Squares*, p. 497, IEP, New York.

Nadeau, R. M., and T. V. McEvilly (1999), Fault slip rates at depth from recurrence intervals of repeating microearthquakes, *Science*, *285*(5428), 718–721.

Nadeau, R. M., and T. V. McEvilly (2004), Periodic pulsing of characteristic microearthquakes on the San Andreas fault, *Science*, *303*, doi:10.1126/science.1090353.

O'leary, D. P. (1990), Robust regression computation using iteratively reweighted least-squares, *SIAM J. Matrix Anal. Appl.*, *11*(3), 466–480.

Parsons, T. (2002), Post-1906 stress recovery of the San Andreas fault system calculated from three-dimensional finite element analysis, *J. Geophys. Res.*, *107*(B8). doi:10.1029/2001JB001051.

Pepe, A., E. Sansosti, P. Berardino, and R. Lanari (2005), On the generation of ERS/ENVISAT DInSAR time-series via the SBAS technique, *IEEE Geosci. Remote Sens. Lett.*, *2*, doi:10.1109/LGRS.2005.848497.

Sandwell, D., R. Mellors, X. Tong, M. Wei, and P. Wessel (2011), Open radar interferometry software for mapping surface deformation, *Eos Trans. AGU*, *92*. doi:10.1029/2011EO280002.

Savage, J. C., and M. Lisowski (1993), Inferred depth of creep on the Hayward Fault, Central California, *J. Geophys. Res. Solid Earth*, *98*(B1), 787–793.

Schaff, D. P., G. H. R. Bokelmann, G. C. Beroza, F. Waldhauser, and W. L. Ellsworth (2002), High-resolution image of Calaveras Fault seismicity, *J. Geophys. Res.*, *107*(B9).

Schmidt, D. A., and R. Bürgmann (2008), Predicted reversal and recovery of surface creep on the Hayward fault following the 1906 San Francisco earthquake, *Geophys. Res. Lett.*, *35*, doi:10.1029/2008GL035270.

Schmidt, D. A., R. Bürgmann, R. M. Nadeau, and M. d'Alessio (2005), Distribution of aseismic slip rate on the Hayward fault inferred from seismic and geodetic data, *J. Geophys. Res.*, *110*. doi:10.1029/2004JB003397.

Segall, P., and R. Harris (1987), The earthquake deformation cycle on the San Andreas fault near Parkfield, California, *J. Geophys. Res.*, *92*, 10,511–10,525.

Shanker, P., F. Casu, H. A. Zebker, and R. Lanari (2011), Comparison of persistent scatterers and small baseline time-series InSAR results: A case study of the San Francisco Bay Area, *IEEE Geosci. Remote Sens. Lett.*, *8*, 592–596, doi:10.1109/LGRS.2010.2095829.

Shirzaei, M. (2012), A wavelet based multitemporal DInSAR algorithm for monitoring ground surface motion, *GRSL*, *10*(3), 456–460, doi:10.1109/LGRS. 2012.2208935.

Shirzaei, M., and R. Bürgmann (2012), Topography correlated atmospheric delay correction in radar interferometry using wavelet transforms, *Geophys. Res. Lett.*, *39*, doi:10.1029/2011GL049971.

Shirzaei, M., and T. R. Walter (2009), Randomly iterated search and statistical competency (RISC) as powerful inversion tools for deformation source modeling: Application to volcano InSAR data, *J. Geophys. Res.*, *114*, B10401, doi:10.1029/2008JB006071.

Shirzaei, M., and T. R. Walter (2010), Time-dependent volcano source monitoring using interferometric synthetic aperture radar time series: A combined genetic algorithm and Kalman filter approach, *J. Geophys. Res.*, *115*. doi:10.1029/2010JB007476.

Shirzaei, M., and T. R. Walter (2011), Estimating the effect of satellite orbital error using wavelet based robust regression applied to InSAR deformation data, *IEEE Trans. Geosci. Rem. Sens.*, *49*, doi:10.1109/TGRS.2011.2143419.

Simpson, R. W., J. J. Lienkaemper, and J. S. Galehouse (2001), Variations in creep rate along the Hayward Fault, California, interpreted as changes in depth of creep, *Geophys. Res. Lett.*, *28*(11), doi:10.1029/2001GL012979.

Toppozada, T. R., and G. Borchardt (1998), Re-evaluation of the 1836 "Hayward fault" and the 1838 San Andreas fault earthquakes, *Bull. Seismol. Soc. Am.*, *88*(1), 140–159.

Vanicek, P., and E. Krakiwesky (1982), *Geodesy: The Concepts*, 697 pp., North-Holand Publishing Co., Amsterdam, The Netherlands.

Wahba, G. (1977), Practical approximate solutions to linear operator equations when data are noisy, *SIAM J. Numer. Anal.*, *14*(4), 651–667.

Waldhauser, F., and W. L. Ellsworth (2002), Fault structure and mechanics of the Hayward Fault, California, from double-difference earthquake locations, *J. Geophys. Res.*, *107*(3), ESE 3–1 to ESE 3–15, doi:10.1029/2000JB000084.

Wyss, M. (2001), Locked and creeping patches along the Hayward Fault, California, *Geophys. Res. Lett.*, *28*(18), 3537–3540.

Yu, E., and P. Segall (1996), Slip in the 1868 Hayward earthquake from the analysis of historical triangulation data, *J. Geophys. Res. Solid Earth*, *101*(B7), 16,101–16,118.

1   **Supplement for**

2

3

4   **Time-dependent model of creep on the Hayward fault**

5   **from joint inversion of 18 years of InSAR and surface**

6   **creep data**

7

8

9

10   **M. Shirzaei[1,2] and R. Bürgmann[2]**

11

12   [1]School of Earth and Space Exploration, Arizona State University, Tempe, AZ 85287-6004,

13   Correspondence: shirzaei@asu.edu, Tel: +1 480 727 4193, fax: +1 480 965 8102

14   [2]Department of Earth and Planetary Science, University of California, Berkeley, California,

15   USA, Correspondence: shirzaei@asu.edu, Tel: +1 480 727 4193, fax: +1 480 965 8102

16
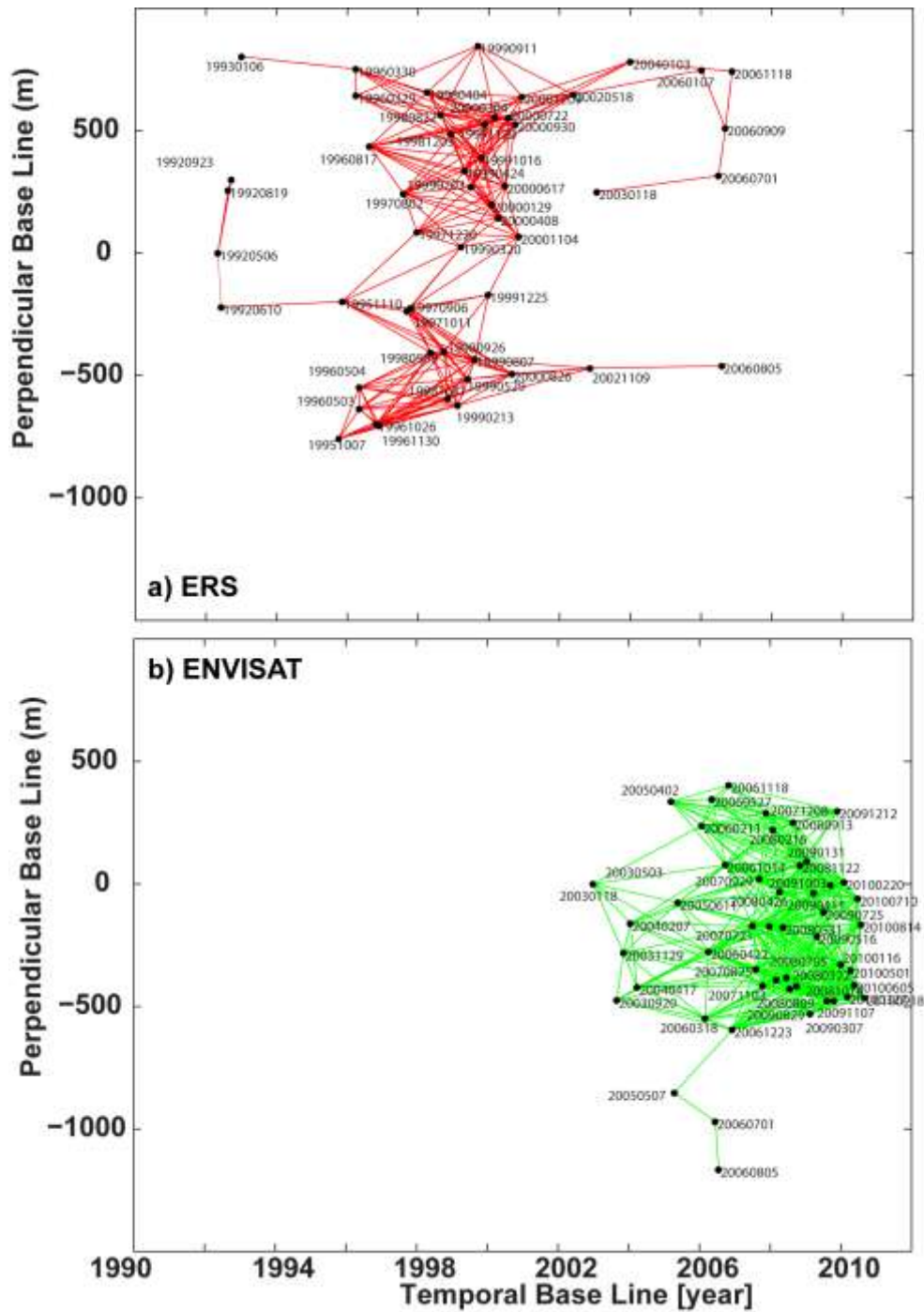
Figure S1: Baseline plot for the ERS (a) and Envisat data (b). Numbers indicate the date of the SAR acquisitions.
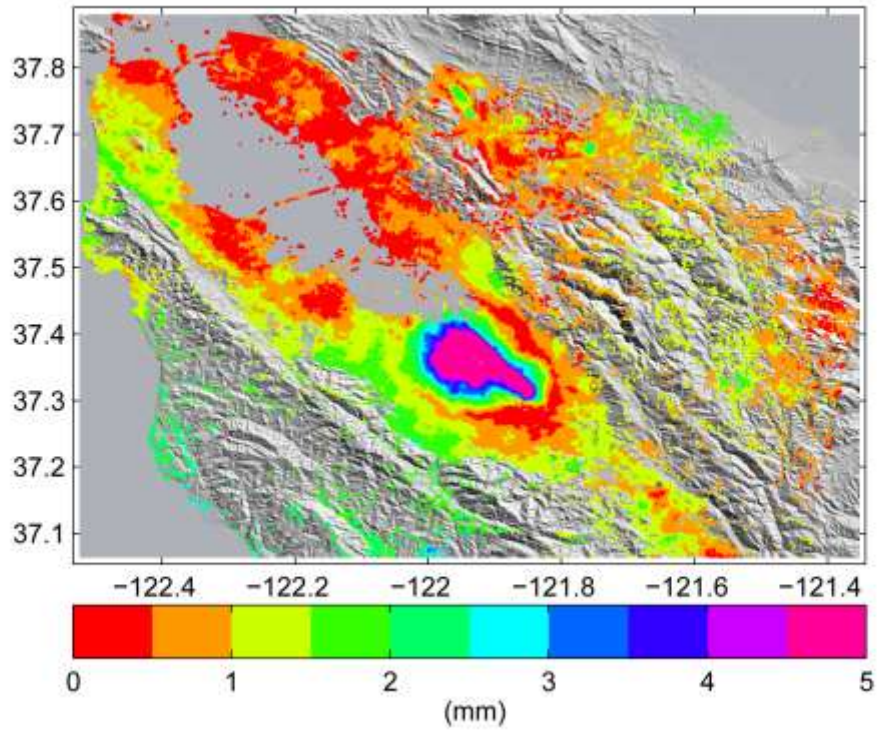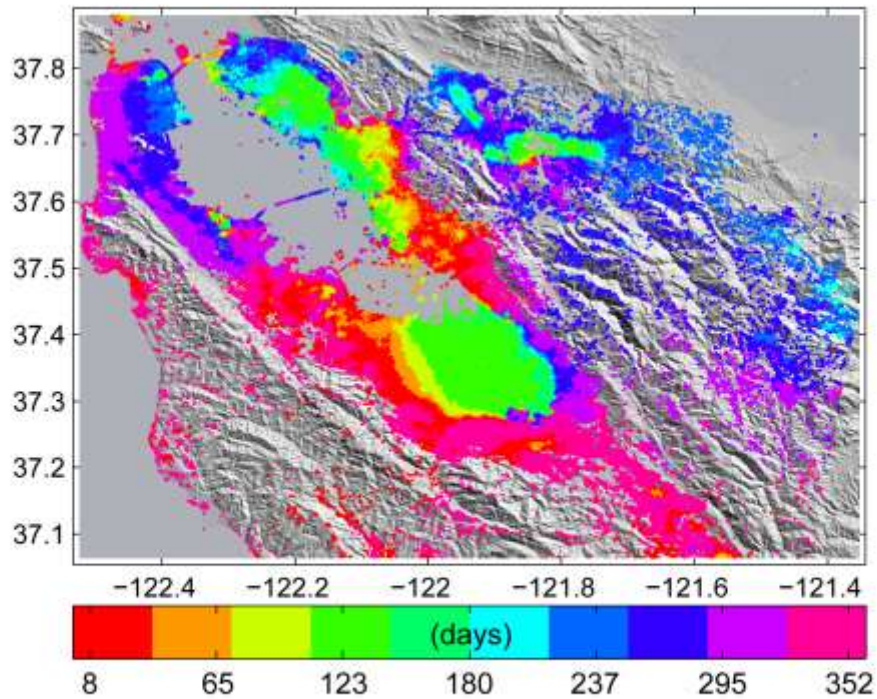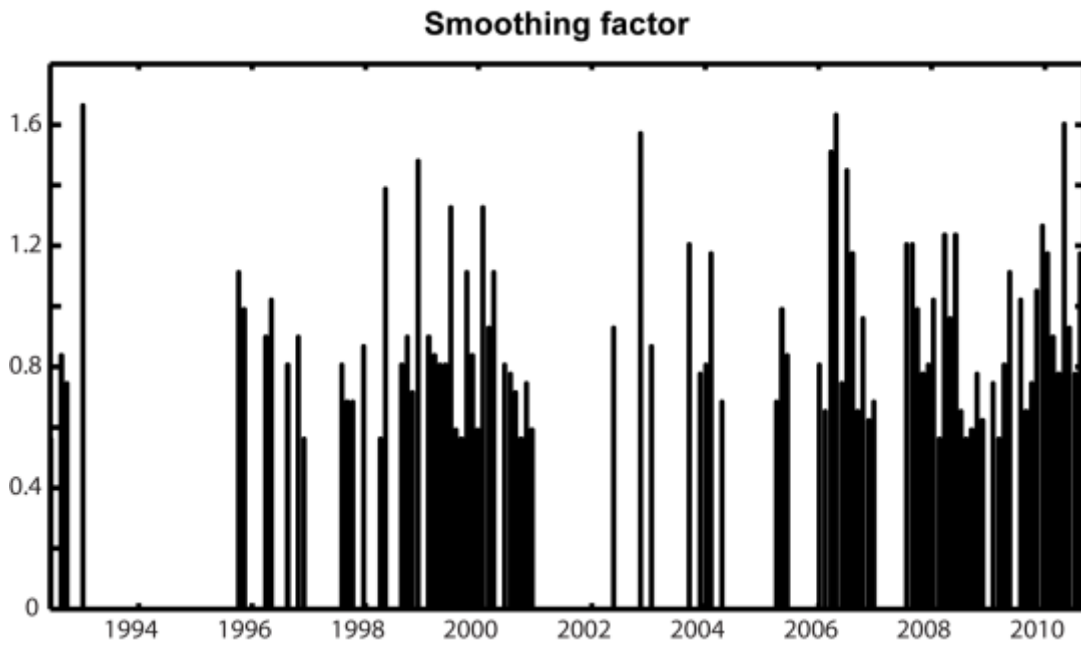
a) Amplitude

b) Phase

Figure S2: Parameters of the annual component removed from the InSAR time series of every stable pixel. a) Amplitude, b) Phase, i.e. the time of year of the peak amplitude.
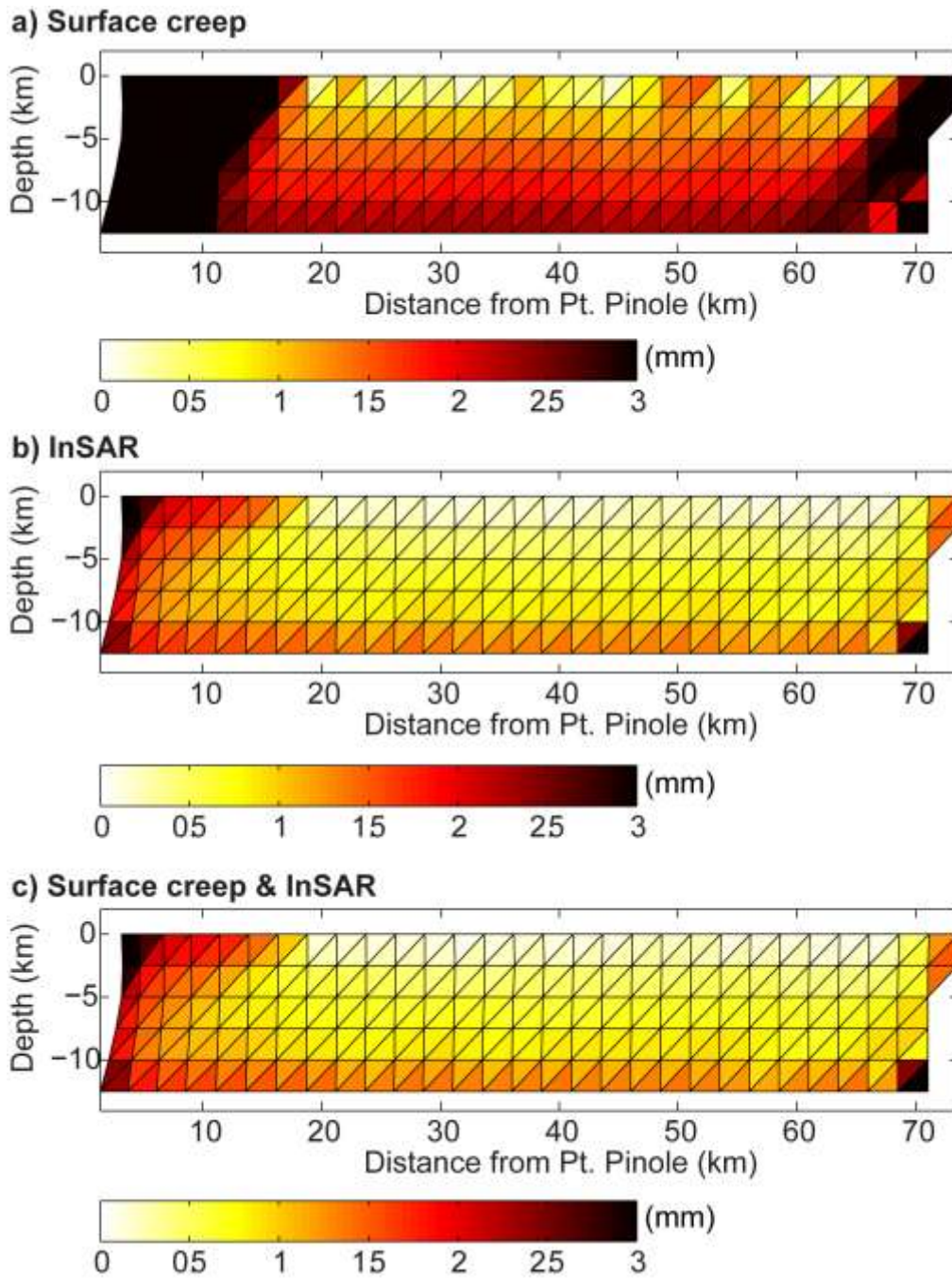
Smoothing factor

27

28

29   **Figure S3:** Time series of smoothing factor obtained following the automatic method detailed

30   in section (2-3).

31

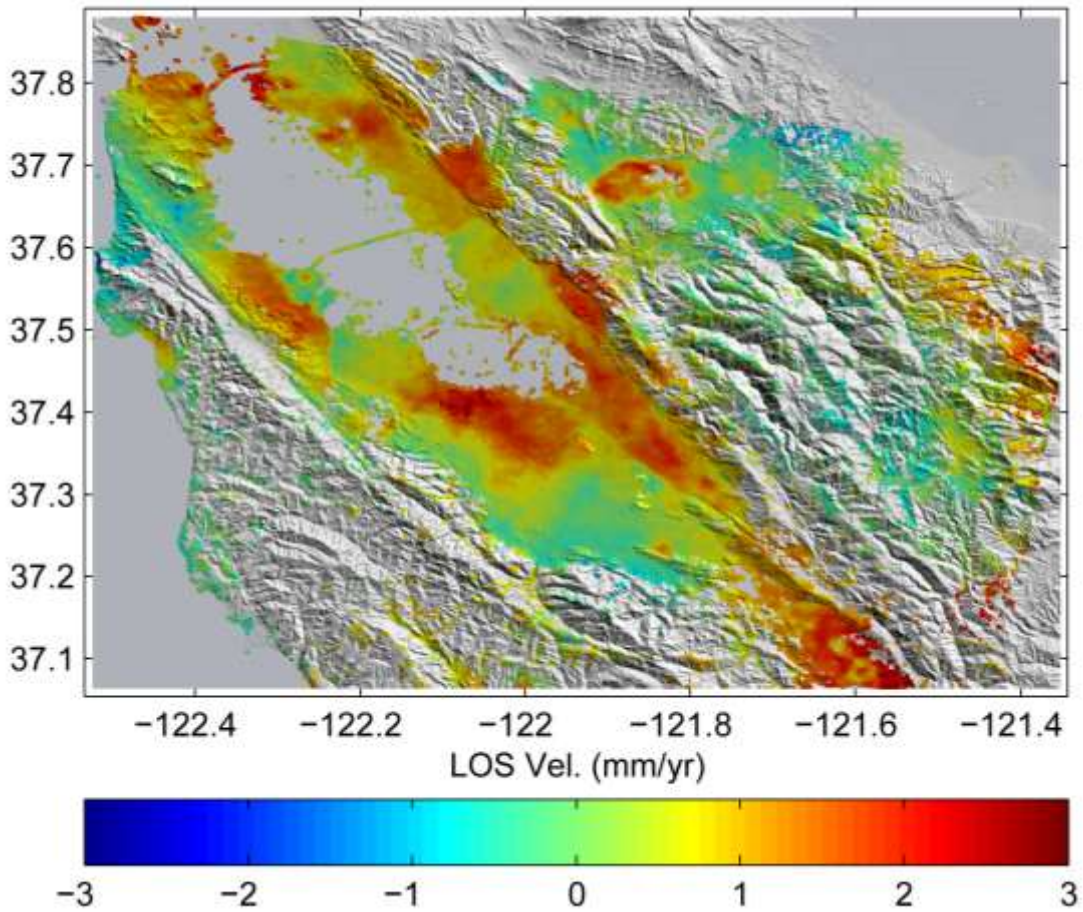**Figure S4:** The results of model resolution test, provided in terms of the standard deviation of the resolved fault creep using only the surface creep data (a) only the InSAR data (b) and the combination of InSAR and surface creep data (c).
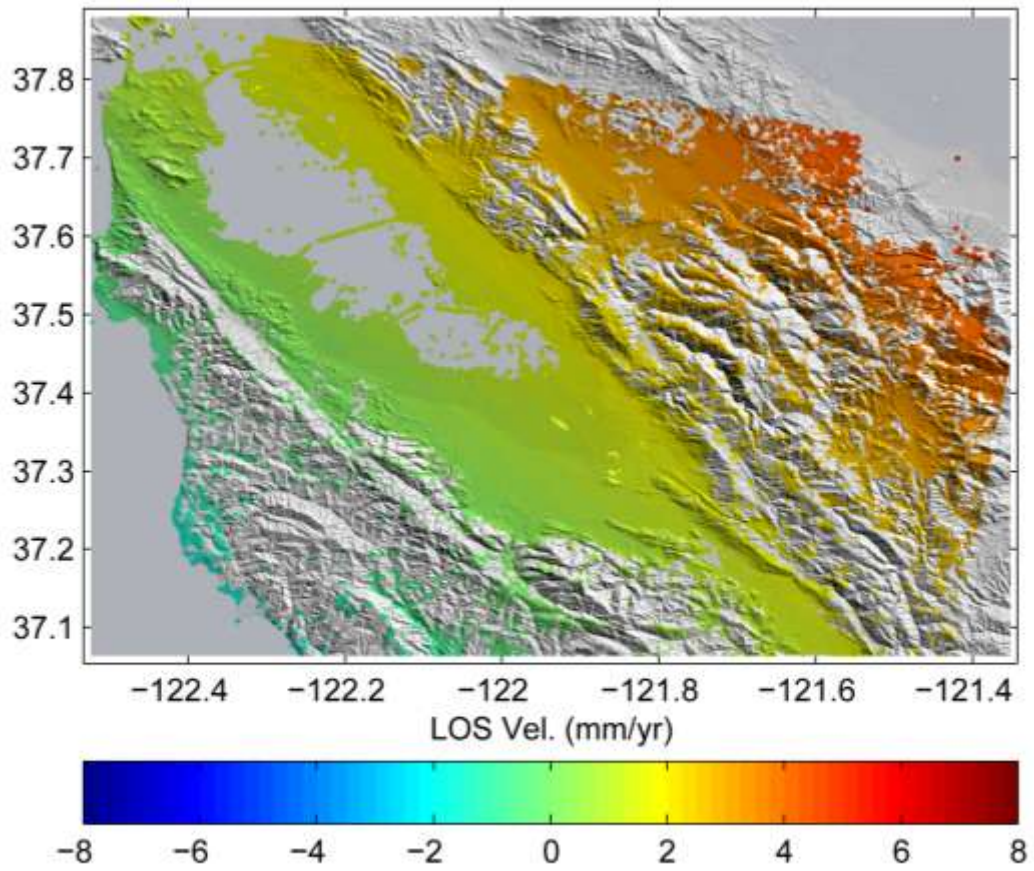
Figure S5: LOS velocity corrected for regional trend determined from GPS-constrained regional dislocation model. Positive LOS velocities (red) indicate movement toward the satellite; i.e., approximately eastward and uplift.
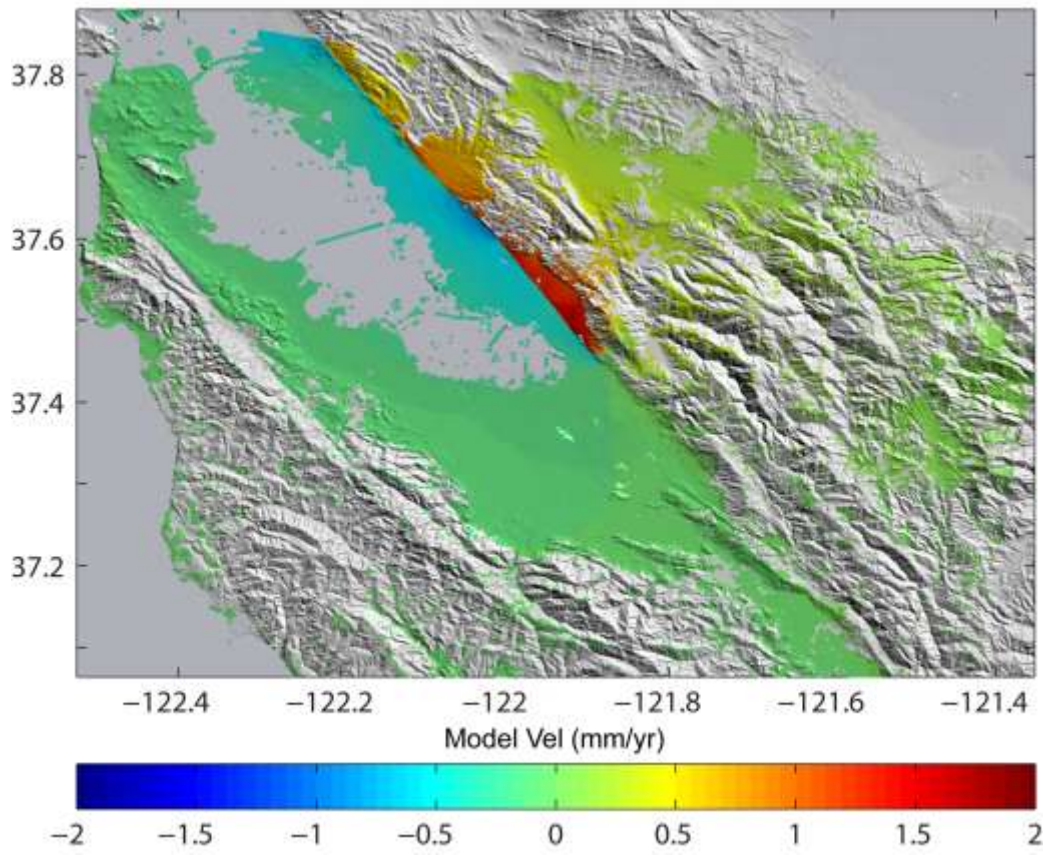
Figure S6: Regional trend used for correcting LOS velocity calculated from dislocation model detailed in Table S1. Red indicates movement toward the satellite.
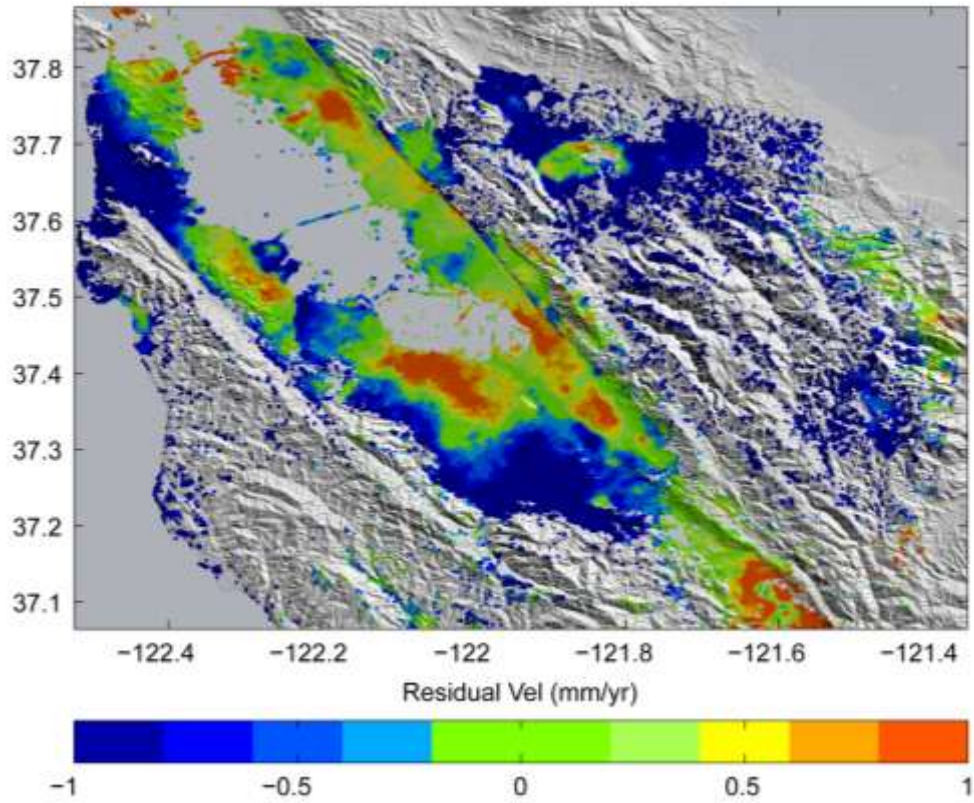
48

Figure S7: The modeled surface displacement velocity obtained in line-of-sight of the Envisat satellite. Red indicates movement toward the satellite.

52

Figure S8: The spatial distribution of the residuals between the Hayward fault creep rate model and the LOS linear velocity of the surface deformation (observed – predicted average LOS velocity). Red indicates movement toward the satellite.

59 **Table S1**: Dislocation model parameters cited from *Bürgmann, et al.* [2006] used to compute

60 regional background deformation shown in Figure S6. Strike-slip rates on vertical model

61 faults are inverted from horizontal GPS velocity field. Four shallow dislocations used by

62 *Bürgmann et al.* [2006] to model the Hayward fault creep are not used.

63

Fault segment	Top	Bottom	SE end		NW end		Slip	STD (+/-)
	(km)	(km)	(°N)	(°E)	(°N)	(°E)	(mm/yr)	(mm/yr)
N San Gregorio	12	3000	36.501	-122	37.905	-122.673	3.5	0.9
Greenville	12	3000	37.4	-121.445	37.85	-121.82	3.8	1.6
Conc.-Green Valley	12	3000	37.85	-121.955	70.72	-199.345	20.6	0.9
Mission-Hayward	12	3000	37.356	-121.725	37.754	-122.152	10.3	2.1
N Calaveras	12	3000	37.356	-121.725	37.801	-122	5.9	2.3
Hayw.-Rodgers Creek	12	3000	37.754	-122.152	64.506	-172.041	4.9	1.2
S Calaveras Deep	12	3000	36.678	-121.285	37.356	-121.725	22.8	1.3
S Calaveras Creep	0	6	36.678	-121.285	37.356	-121.725	11	0.8
N SAF	12	3000	37.905	-122.673	41.05	-125.68	21.5	1.5
SAF Peninsula	12	3000	37.23	-122.09	37.905	-122.673	19.5	1
SAF Loma Prieta	12	3000	36.678	-121.285	37.23	-122.09	19.5	1
SAF Transition Creep	0	8	36.678	-121.285	36.86	-121.55	21.5	0.8
S SAF	0	3000	30.44	-115.15	36.678	-121.285	30.7	0.9

64

65

66

References

Bürgmann, R., G. Hilley, A. Ferretti, and F. Novali (2006), Resolving vertical tectonics in the San Francisco Bay Area from permanent scatterer InSAR and GPS analysis, *Geology*, *34*, 3, 221-224.